Supplementary Information

Charge Recombination in Polythiophene:Non-Fullerene Acceptor Solar Cells with IE Offsets Exceeding 1 eV†

Wejdan Althobaiti*[a], Julien Gorenflot*[a], Catherine S. P. De Castro[a], Jafar I. Khan[a], Christopher E. Petoukhoff[a], Shahidul Alam[a,d], Oleksandr Matiash[a], Yakun He[a], George T. Harrison[a], Anirudh Sharma[a], Weimin Zhang[a], Valentina Musteata[b], José P Jurado[a], Marco Marengo[a], Derya Baran[a], Stefaan De Wolf[a], Iain McCulloch[c], Shadi Fatayer[a], and Frédéric Laquai*[a,d]

[a]King Abdullah University of Science and Technology (KAUST), KAUST Solar Platform (KSP), Physical Sciences and Engineering Division (PSE), Thuwal 23955-6900, Kingdom of Saudi Arabia.

[b]King Abdullah University of Science and Technology, Imaging and Characterization Core Lab, Thuwal 23955-6900, Kingdom of Saudi Arabia.

[c]University of Oxford, Department of Chemistry, Oxford, UK.

[d]Chair of Physical Chemistry and Spectroscopy of Energy Materials, Department of Chemistry, Ludwig-Maximilians-University (LMU) Munich, Butenandtstraße 5-13, 81377 Munich, Germany

*Correspondence: wejdan.althobaiti@kaust.edu.sa
*Correspondence: julien.gorenflot@kaust.edu.sa
*Correspondence: frederic.laquai@kaust.edu.sa

Present Address: J.I.K: University of Hull, Department of Physics, HU6 7RX, Hull, UK.

Contents

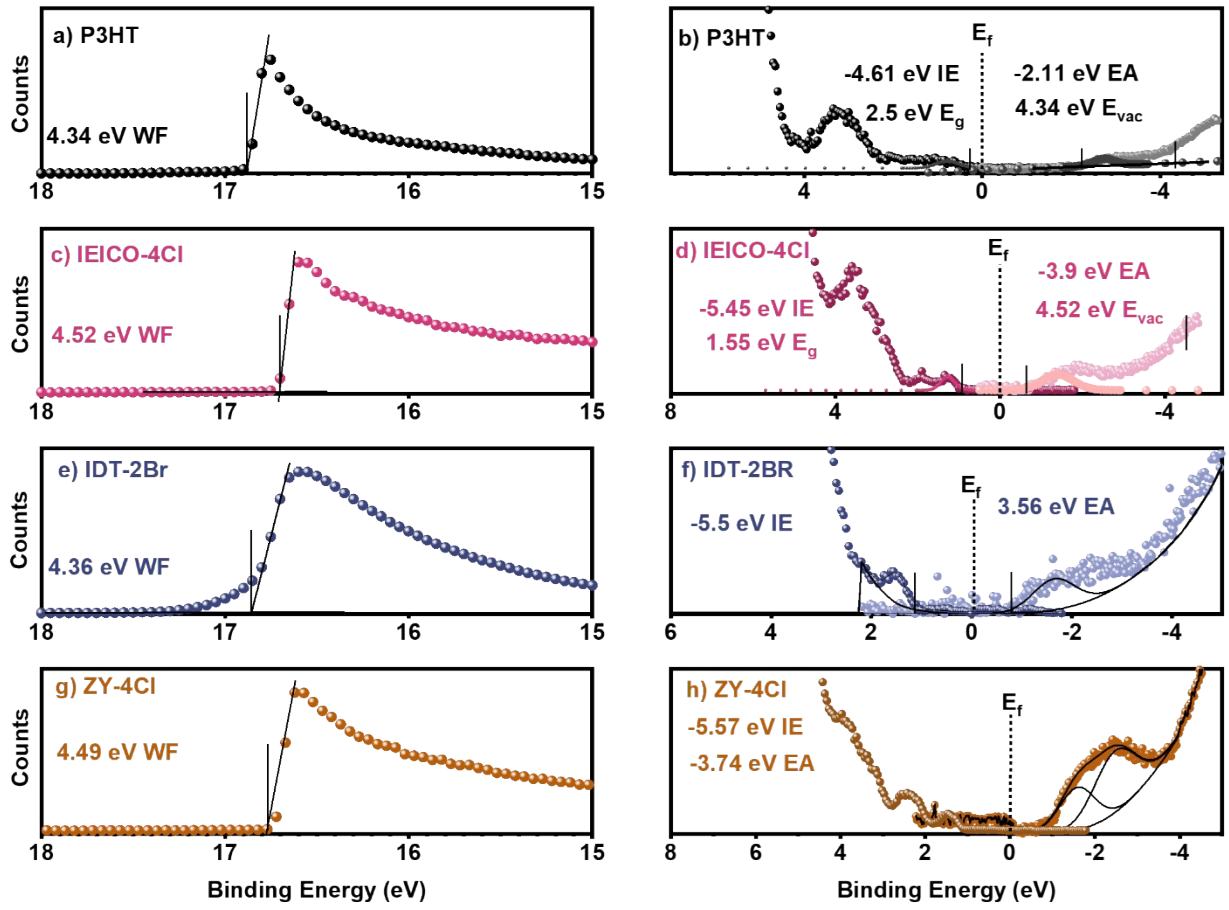

UPS and IPES

Fig. S1: Ionization energy (IE) and electron affinity (EA) from ultraviolet photoelectron (UPS) and low-energy inverse photoelectron (IPES) spectroscopy for a-b) P3HT, c-d) IEICO-4Cl, e-f) IDT-2Br, and g-h) ZY-4Cl.

PESA

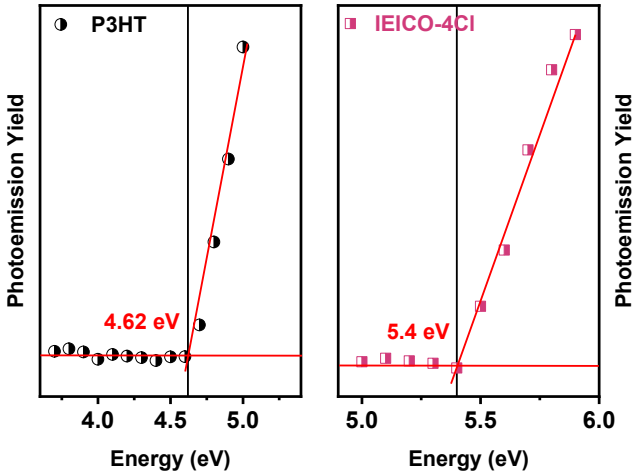

Fig. S2: Experimentally determined PESA data of neat donor P3HT and neat IEICO-4Cl films presented by the solid dots and squares respectively. The IE values are extracted upon fitting (solid line) the experimental data.

Ellipsometry

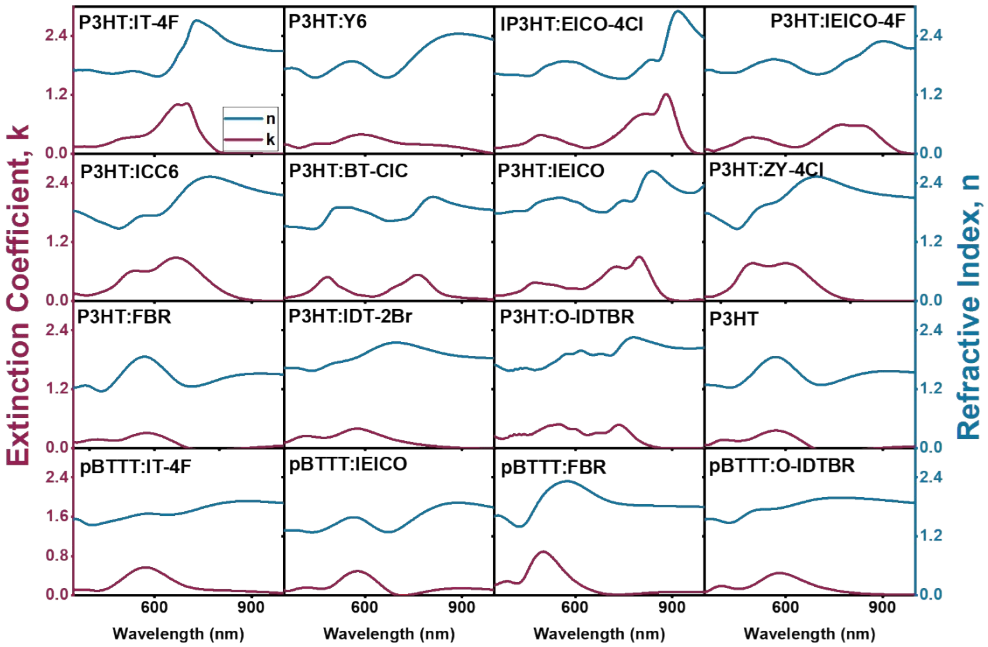

Fig. S3: Extinction coefficient (*k*) (dark pink lines) and refractive indices (*n*) (light blue lines) of blend thin films determined by spectroscopic ellipsometry measurements. For these measurements, the photoactive blends were deposited on a SiOx substrate on a silicon wafer.

Reflectance

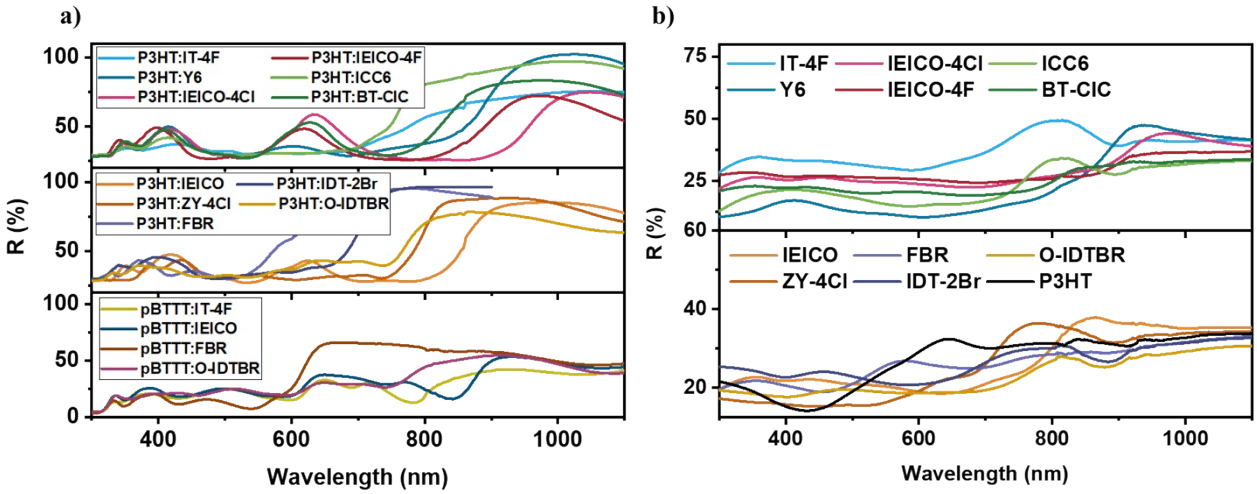

Fig. S4: Reflectance (%R) spectra measured using the integrating sphere for a) full device structure (P3HT:NFAs and pBTTT:NFAs). b) Neat films on glass substrates.

Internal Quantum Efficiency (IQE) Spectra

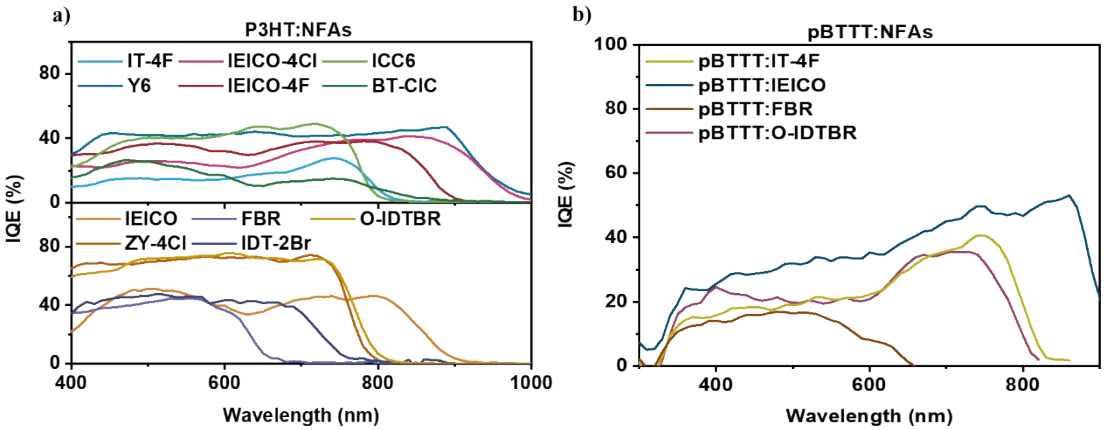

Fig. S5: Internal quantum efficiency (IQE) spectra of the studied a) P3HT:NFAs and b) pBTTT:NFAs organic solar cells.

Table S1: Averaged internal quantum efficiency (IQE_{Avg}) and the spectral range (λ_{Avg}) used for estimating the (IQE_{Avg}).

Donor:NFA	IQE_{Avg} (%)	λ_{Avg} (nm)
P3HT:IT-4F	16.4	400-740
P3HT:Y6	42.82	440-890
P3HT:IEICO-4Cl	29.68	400-860
P3HT:IEICO-4F	34.44	400-800
P3HT:ICC6	42.84	470-720
P3HT:BT-CIC	17.84	400-750
P3HT:IEICO	43.72	480-800
P3HT:ZY-4Cl	70.79	400-720
P3HT:FBR	39.88	400-590
P3HT:IDT-2Br	43.56	400-690
P3HT:O-IDTBR	70.07	400-730
pBTTT:IT-4F	23.64	360-740
pBTTT:IEICO	37.78	360-860
pBTTT:FBR	14.87	360-570
pBTTT:O-IDTBR	25.15	400-730

Large IE and EA offsets

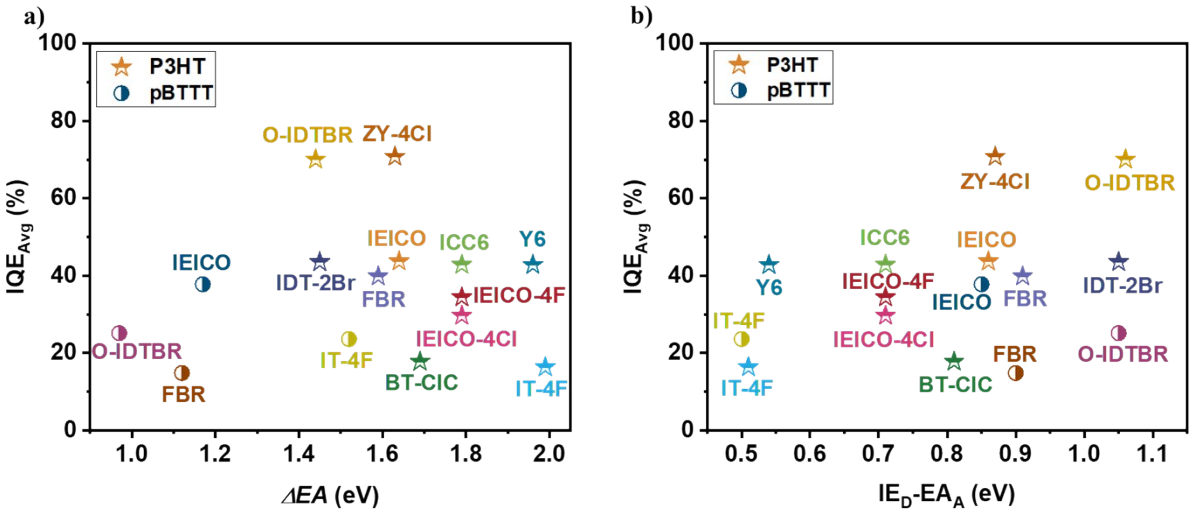

Fig. S6: Averaged IQE (IQE_{Avg}) of Donor:NFA-based devices as a function of a) EA offset (ΔEA), and b) Diagonal Bandgap (IE_D-EA_A).

UV-Vis Spectroscopy

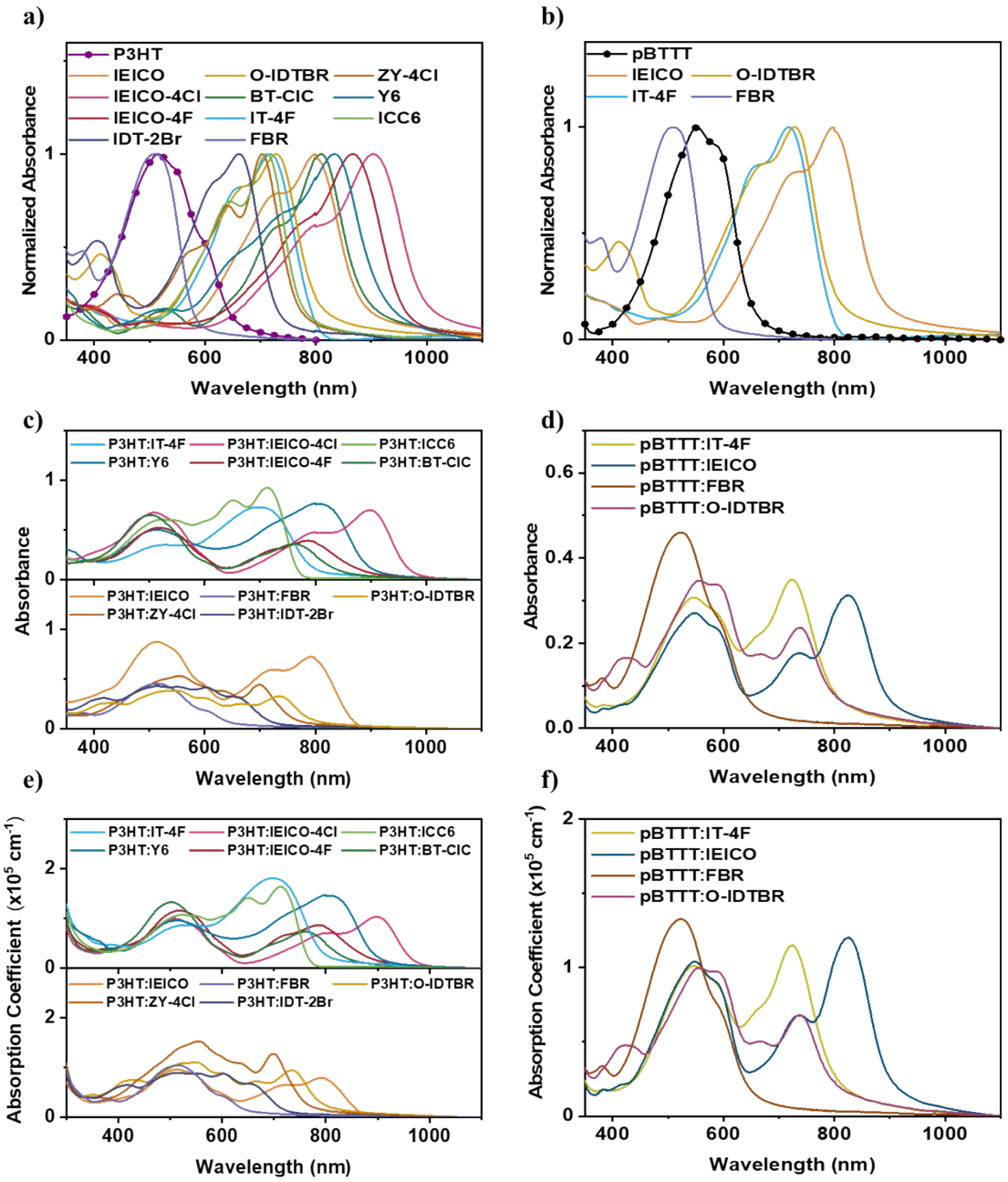

Fig. S7: a-b) Normalized UV-Vis-NIR absorbance spectra of neat donors (P3HT and pBTTT) (line with solid dots) and neat NFA thin films on glass substrates. UV-Vis-NIR absorbance spectra of the photoactive blend thin films on glass substrates of c) P3HT:NFAs based blends and d) pBTTT:NFAs based blends. Absorption coefficient (α_{abs}) spectra of e) P3HT:NFA based blends and f) pBTTT:NFAs based blends.

Optical Bandgap Determination

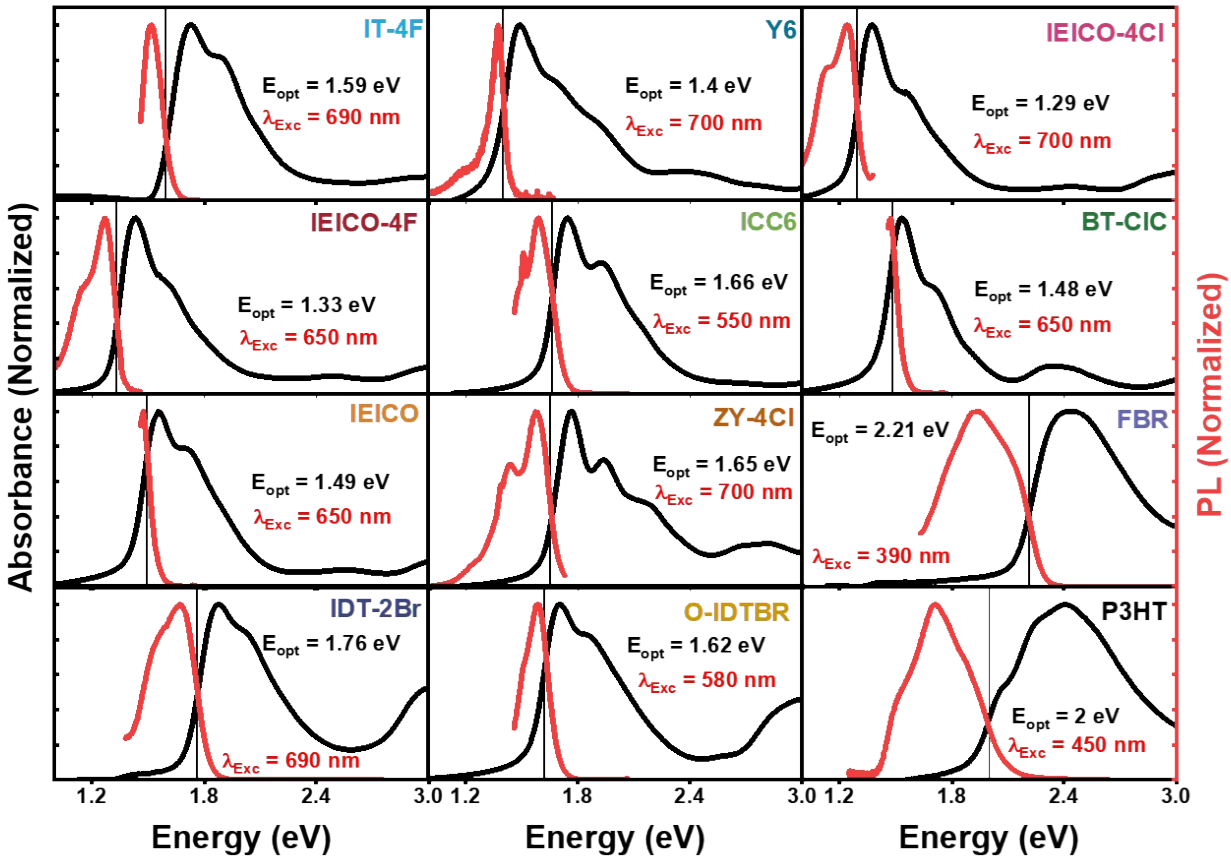

Fig. S8: Normalized absorbance and PL (emission) spectra of neat material films and the estimated optical bandgaps (E_{opt}). The E_{opt} were determined at the intersection of the respective PL (corrected to the sensitivity of the detector) and absorption spectra as indicated by the thin vertical lines. λ_{Exc} is the excitation wavelength.

Device optimization conditions

Table S2: Processing parameters used for optimized OSCs with the total blend concentration, Donor:Acceptor (D:A) blend ratio, solvent used, annealing temperature (T_{ann}), annealing time (t_{ann}), and spin speed on the spin-coater.

Donor:NFA	Concentration (mg/mL)	D:A	Solvent	T_{ann} (°C)	t_{ann} (min)	Speed (rpm)
P3HT:IT-4F	30	1:2	CF+Anisole (8:2) +DIO(2.5%)	160	10	4000
P3HT:Y6	30	1:2	CF	160	10	2500
P3HT:IEICO-4Cl	20	1:1	CF	160	10	2000
P3HT:IEICO-4F	20	1:1	CB	160	15	800
P3HT:ICC6	25	1:1	CF	120	10	2000
P3HT:BT-CIC	20	2:1	CF	160	10	2000
P3HT:IEICO	20	1:1	CF	160	10	2000
P3HT:ZY-4Cl	20	1:1	THF	120	10	2500
P3HT:FBR	25	1:1	CF,oDCB	110	15	2500
P3HT:IDT-2Br	30	1:1	oDCB+CN(3%)	140	10	800
P3HT:O-IDTBR	24	1:1	CB	140	15	2000
pBTTT:IT-4F	20	1:1	CB	150	10	2000
pBTTT:IEICO	20	1:1	CB	150	10	2500
pBTTT:FBR	20	1:1	CB	150	10	2000
pBTTT:O-IDTBR	20	1:1	CB	150	10	1500

Transfer matrix simulation

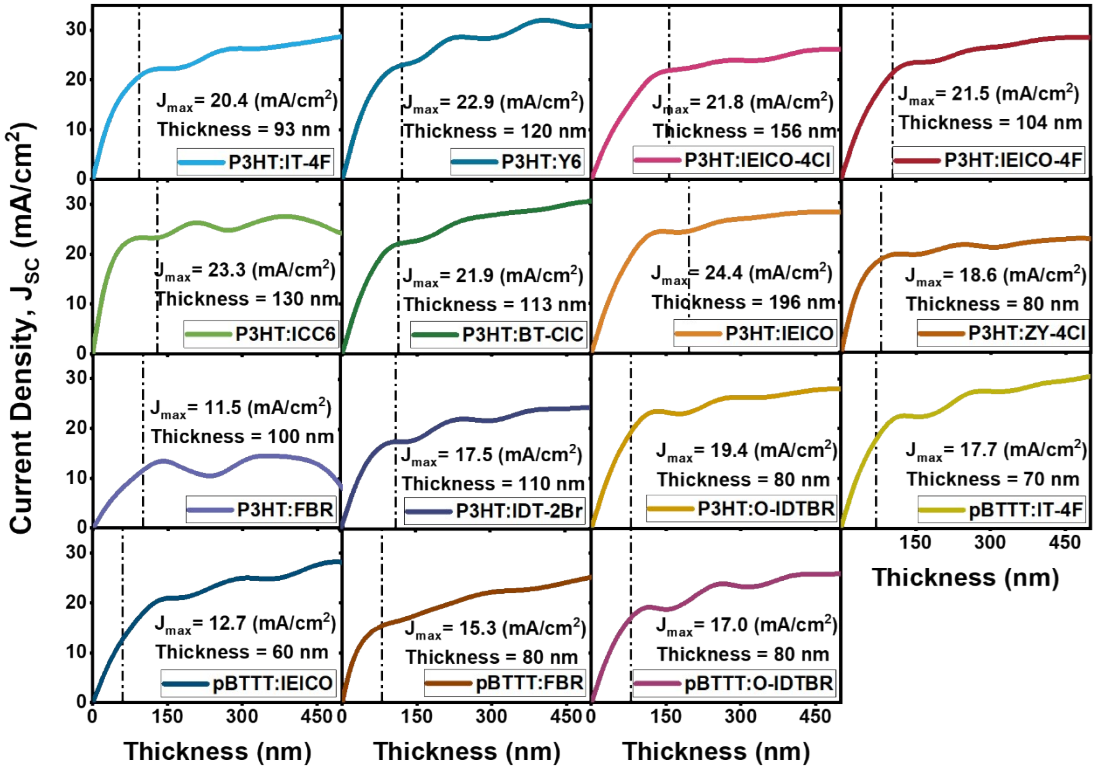

Fig. S9: Maximum simulated short current density ($J_{SC,sim}$) at 100% internal quantum efficiency of Donor:NFAs based devices as a function of the photoactive layer thickness. The experimentally optimized active layer thicknesses are indicated by the dashed line.

Förster Resonance Energy Transfer (FRET) Radii and Rates

To calculate the energy transfer rate (k_{FRET}) between the donor and the acceptot (D-A) separated by distance R we used this equation:

$$k_{FRET} = \frac{1}{\tau_D}\left(\frac{R_0}{R}\right)^6$$

Where, τ_D is the fluorescence lifetime of the donor (from TRPL measurements, **see Table S6**), which is P3HT in this case, in the absence of an acceptor and R_0 is Förster radius.

From the spectral overlap between the emission of P3HT and the absorption of the NFAs we can determine the Förster radius R_0 in nanometers using the equation bellow:

$$R_0 = 0.0211\left(\frac{\kappa^2 \Theta_D J(\lambda)}{n^4}\right)^{\frac{1}{6}}$$

Where, κ^2 is the dipole-dipole statistical orientation factor, Θ_D is the photoluminescence quantum yield (PLQY) of the donor (P3HT), J is the spectral overlap integral between the normalized emission of the donor and the normalized extinction coefficients of the acceptor, n is the refractive index of the bulk heterojunction.

In order to get R_0 in nanometers and J in mol^{-1}.L.cm^{-1}.nm^4, this 0.0211 factor is used and it is equal to:

$$0.0211 = \left(\frac{9ln(10)}{128\pi^5 N_A} \times 10^{17}\right)^{\frac{1}{6}}$$

Where, N_A is Avogadro's number in mol^{-1}, $ln(10)$ is required to convert the common logarithm (decadic logarithm) absorbance to natural logarithm absorbance to calculate the extinction coefficient, 10^{17} to convert L.cm^{-1}.nm^4 in J to nm^6 in ${R_0}^6$.[1]

The mechanism of FRET is based on the statistical coupling of the dipoles of the donor and the acceptor. Therefore, the dipoles need to have a favorable orientation between each other for the energy transfer to take place. κ^2 values can be assumed from 0 to 4 based on the orientation of the dipoles. In this study we used $\kappa^2 = 0.476$ which is the assumption when the dipoles have random orientation in fixed time (solid films).[2,3]

Finally, we calculated the integrated spectral overlap $J(\lambda)$ in $mol^{-1}.L.cm^{-1}.nm^4$ (we use $J(\lambda)$ not J because we integrated over wavelengths not wavenumbers) between the extinction coefficient of the acceptor (NFA) and the emission of the donor (P3HT) using this equation:

$$J(\lambda) = \int_0^\infty \varepsilon_A(\lambda)\lambda^4 F_D(\lambda)d\lambda$$

Where, $\varepsilon_A(\lambda)$ is the acceptor's molar extinction coefficient in $cm^{-1}.mol^{-1}.L$, λ is the wavelength in nm, $F_D(\lambda)$ is the emission spectrum of donor (P3HT).

The effective refractive index n_{eff} can be calculated as amplitude-weighted of the spectral overlap using the equation below:

$$n_{eff} = \frac{\int_0^\infty \varepsilon_A(\lambda)n(\lambda)\lambda^4 F_D(\lambda)d\lambda}{J(\lambda)}$$

Where, $n(\lambda)$ is the refractive index spectra of the blend films were obtained from spectroscopic ellipsometry (see Figure S3).

Since we used thin films in our measurements, we calculated the extinction coefficient of the NFAs, $\varepsilon_A(\lambda)$, with this equation:

$$\varepsilon(\lambda) = \frac{\alpha(\lambda).M_w}{d}$$

Where, $\alpha(\lambda)$ is the absorption coefficient in cm^{-1} calculated from the common logarithm absorbance from Beer-Lambert law (with taking the reflection into consideration[4]), M_w is the molecular weight, and density[5] d of 1200 g/L used for all the materials, except for P3HT where the actual value of the density were used ($d = 1100$ g/L)[6].

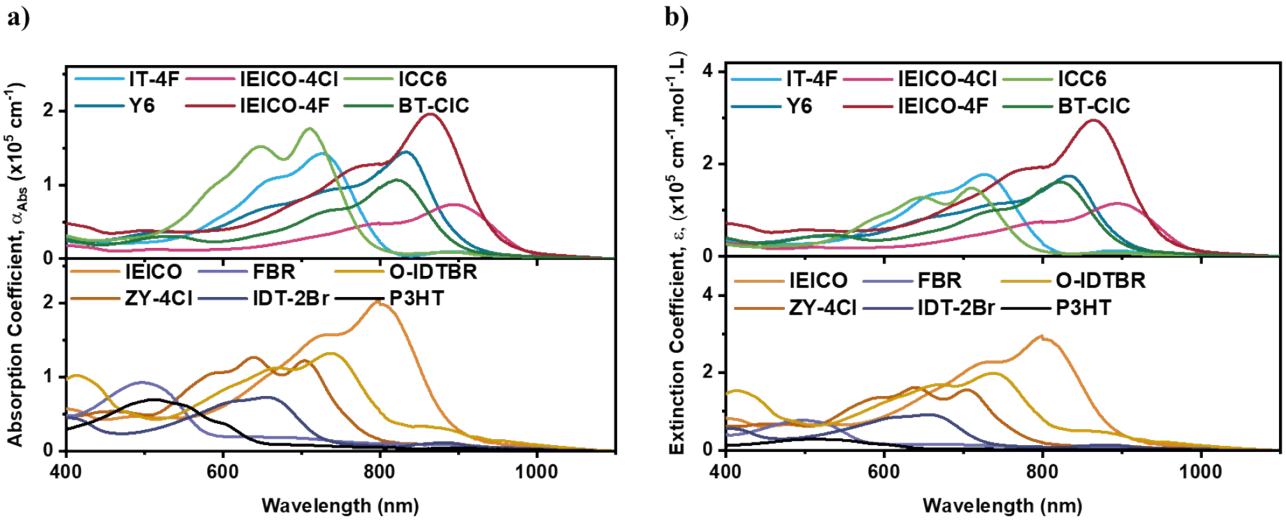

Fig. S10: a) Absorption coefficient (α_{Abs}) and b) extinction coefficient (ε) of P3HT:NFA blends in films.

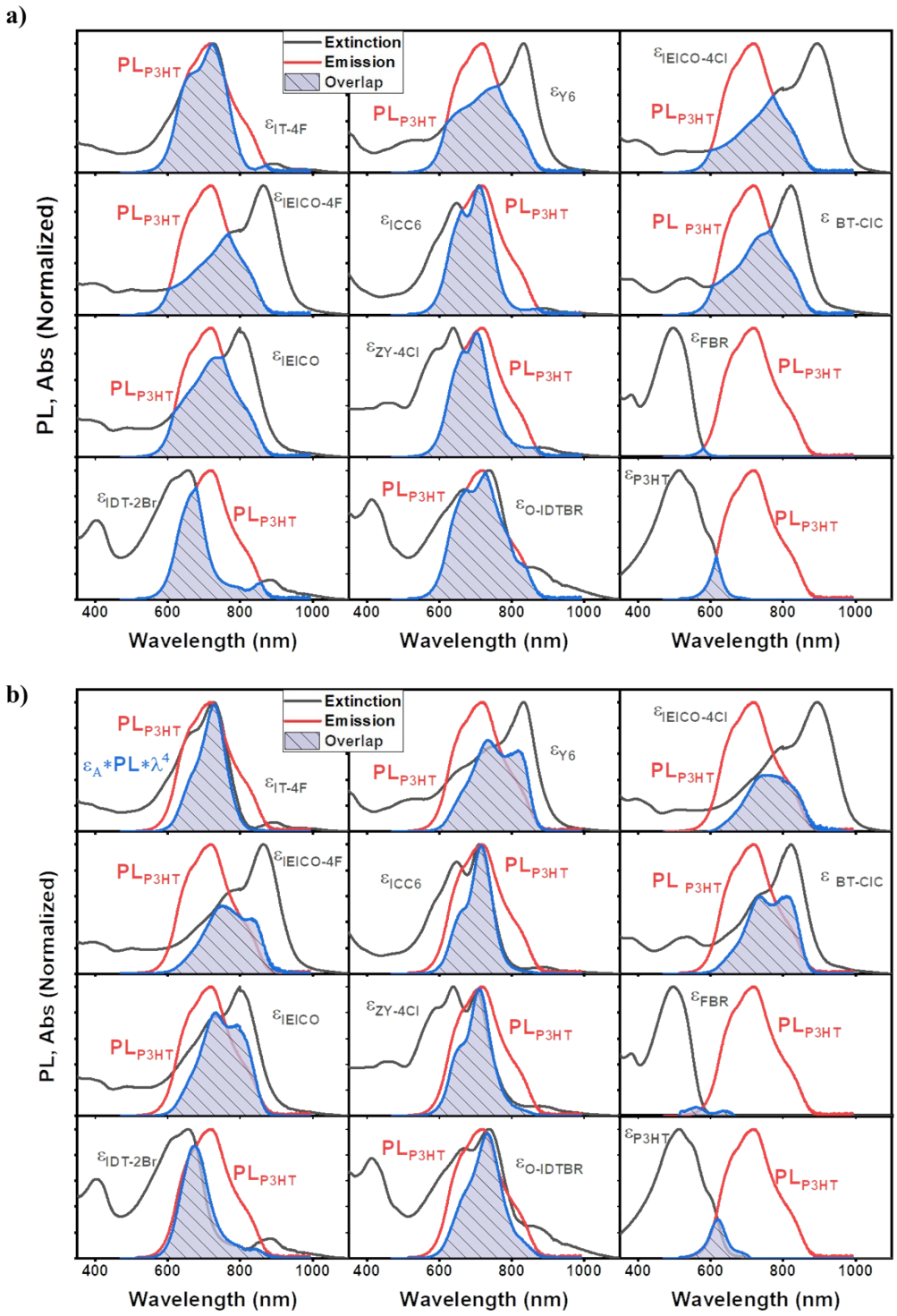

Fig. S11: a) Spectral overlap between normalized PL of P3HT ($\lambda_{Exc} = 450\ nm$) and normalized extinction coefficient of neat materials. b) Visualization of the overlap integral $J = \int \varepsilon_A \times PL \times \lambda^4$ also used to calculate the amplitude weighted average refractive index n_{eff}.

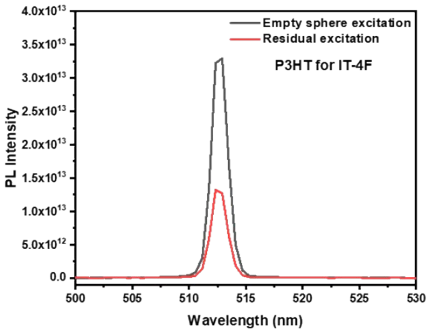
Empty sphere excitation
Residual excitation
P3HT for IT-4F
PL Intensity
Wavelength (nm)

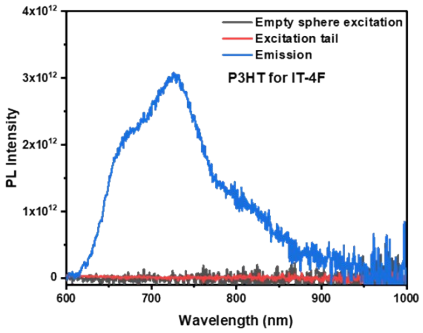
Empty sphere excitation
Excitation tail
Emission
P3HT for IT-4F
PL Intensity
Wavelength (nm)

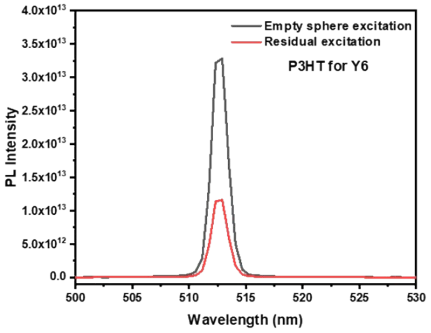
Empty sphere excitation
Residual excitation
P3HT for Y6
PL Intensity
Wavelength (nm)

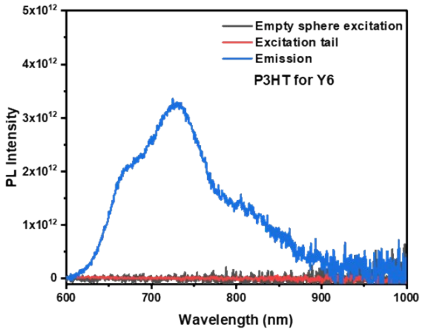
Empty sphere excitation
Excitation tail
Emission
P3HT for Y6
PL Intensity
Wavelength (nm)

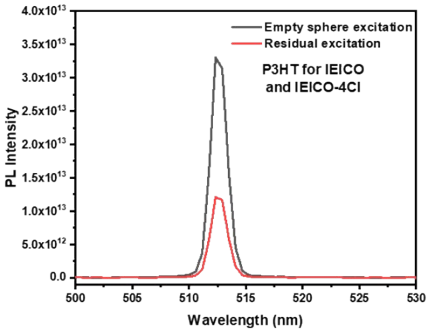
Empty sphere excitation
Residual excitation
P3HT for IEICO
and IEICO-4Cl
PL Intensity
Wavelength (nm)

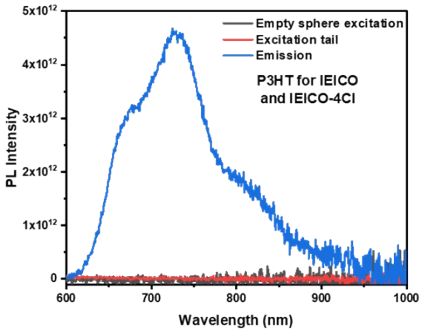
Empty sphere excitation
Excitation tail
Emission
P3HT for IEICO
and IEICO-4Cl
PL Intensity
Wavelength (nm)

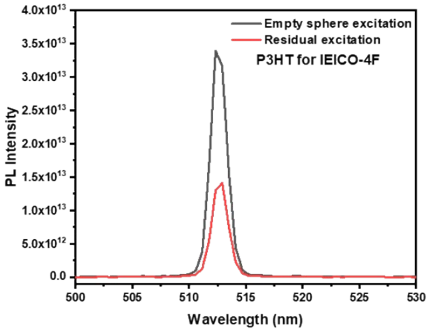
Empty sphere excitation
Residual excitation
P3HT for IEICO-4F
PL Intensity
Wavelength (nm)

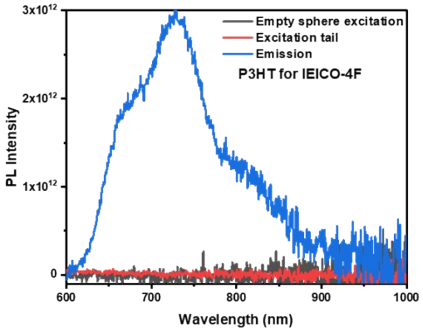
Empty sphere excitation
Excitation tail
Emission
P3HT for IEICO-4F
PL Intensity
Wavelength (nm)

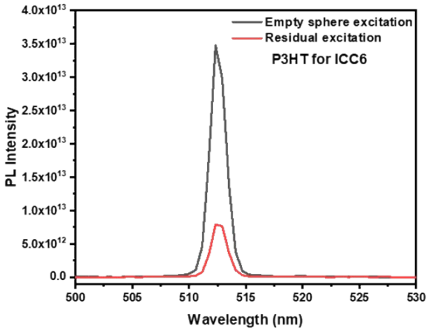
Empty sphere excitation
Residual excitation
P3HT for ICC6
PL Intensity
Wavelength (nm)

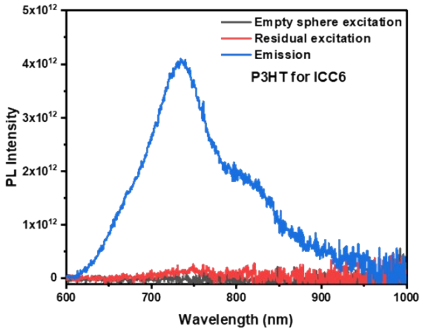
Empty sphere excitation
Residual excitation
Emission
P3HT for ICC6
PL Intensity
Wavelength (nm)

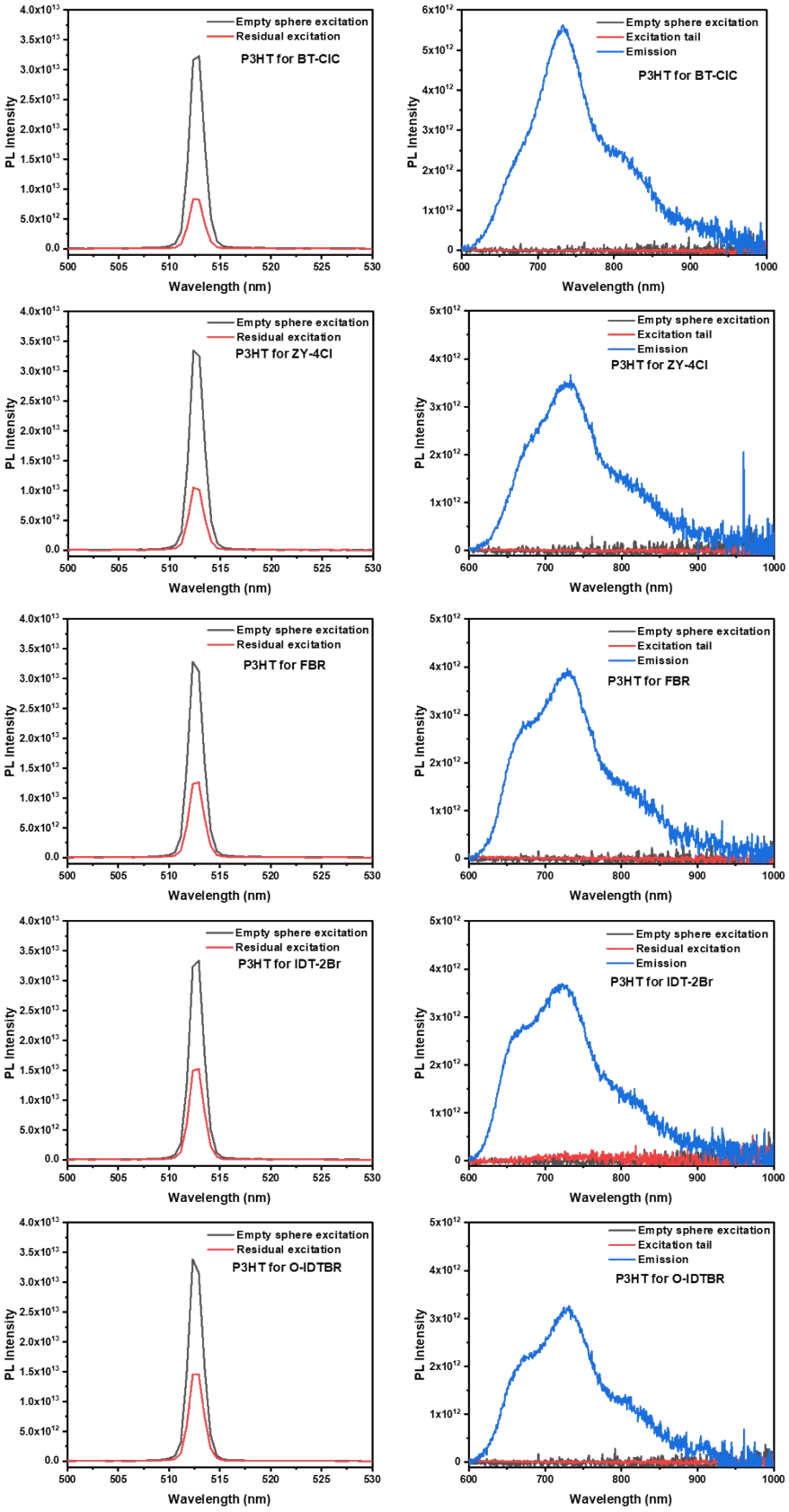

Fig. S12: PL spectra for different processing conditions for P3HT to calculate the PLQY (Θ_D). PLQY measurements were done in integrated sphere in N_2 environment.

Photoluminescence quantum yield (PLQY) measurements of P3HT films were performed inside a nitrogen-filled glovebox using a visible-range PLQY setup. Excitation was provided by a Cobolt MLD-06-01 laser operating at 515 nm with a power of 4.2 mW and a beam cross-section of 2.722 × 2.689 mm² (0.0575 cm²). The emitted and transmitted signals were collected using an Avantes AvaSpec-ULS2048XL-EVO spectrometer with an integration time of 1000 ms and 20 averages per measurement. The routine included background correction by recording and subtracting the dark signal, as well as an empty sphere measurement of the excitation beam (OD 2 filter applied), residual excitation measurement of the non-absorbed laser signal (OD 2 filter applied), and the emission spectrum of the sample with a long-pass LP550 filter to block scattered excitation light. An optional correction was also applied by measuring the non-filtered shoulder of the excitation peak overlapping with the emission spectrum, using the same LP550 filter.

PLQY calculation:

- Excitation peak integration boundaries ($^{A_{ex}}$,$^{A_{ex-em}}$): 500…530 nm
- Emission peak integration boundaries ($^{A_{em-corr}}$): 600…950 nm
- Excitation tail integration boundaries ($^{A_{tail-ex}}$,$^{A_{tail-ex-em}}$): 555…600 nm
- Tail scaling factor: $F_{tail} = \frac{A_{tail-ex-em}}{A_{tail-ex}}$
- Tail subtraction: $I_{em-corr}(\lambda) = I_{em}(\lambda) - F_{tail} \cdot I_{tail}(\lambda)$
- PLQY calculation:

$$PLQY = \frac{A_{em-corr}}{\frac{1}{\%T}(A_{ex} - A_{ex-em})}$$

Table S3: Energy transfer input parameters and results. M_w is the molecular weight, κ^2= 0.476[2,3], PLQY for P3HT (Θ_D) (see Figure S12), n_{eff} amplitude weighted average value of the refractive index of the blend. $J(\lambda)$ is the overlap integral between the absorption of the acceptor and the emission of the donor. R_0 is the Förster radius, which is the distance between D-A, k_{FRET} is the energy transfer rate.

BLEND (P3HT:A)	M_w (g/mol)	n_{eff}	Θ_D (%)	J(λ) ($\times 10^{13}$ mol^{-1} L cm^{-1} nm^4)	R_0 (nm)	k_{FRET} (1 nm) ($\times 10^{12}$ s^{-1})
IT-4F	1499.9	2.06	7.1	2920	4.10	6.81
Y6	1451.9	2.01	7.1	3130	4.22	6.88
IEICO-4Cl	1874.2	2.11	10.1	1550	3.85	3.97
IEICO-4F	1808.4	2.1	7	4370	4.32	9.70
ICC6	1011.3	2.1	7	2100	3.84	3.60
BT-CIC	1822.1	1.86	9.8	2700	4.58	10.5
IEICO	1736.4	2.13	10.1	5800	4.76	14.2
ZY-4Cl	1533.8	2.2	7	2390	3.79	4.11
FBR	1001.4	1.5	9	3.31	1.70	0.032
IDT-2Br	1518.2	1.93	9.9	930	3.74	4.32
O-IDTBR	1326.0	1.98	8	3920	4.52	11.8
P3HT	498[a]	1.53	8.23[c]	17	2.17	0.128

[a] Molecular weight of 3 monomer units of P3HT based on coherence length equal to 1.1 nm.[7]
[b] The density of P3HT.[8]

[c] Average PLQY value measured for P3HT across different processing conditions.

We used Python code to calculate n_{eff}, $J(\lambda)$,R_0, and k_{FRET}.[9]

Time-Resolved Photoluminescence (TRPL)

TRPL follows $A_1 e^{\frac{-t}{\tau_1}} + A_2 e^{\frac{-t}{\tau_2}}$, and PL is the radiative part of $\frac{dn_{excitons}}{dt}$. Assuming that the radiative fraction of recombination remains the same over the decay, $dn_{exciton}/dt\ (t)$ is thus proportional to PL(t). Note that this assumption neglects second order exciton decay processes, as well as exciton relaxation, which would likely affect the radiative yield.

➔ Integration yields:

$$n_{exciton}(t) = n_0\left[1 - \frac{A_1}{\tau_1} e^{\frac{-t}{\tau_1}} - \frac{A_2}{\tau_2} e^{\frac{-t}{\tau_2}}\right]$$

➔ Hence the average exciton lifetime is the intensity-averaged exciton lifetime (τ_{avg}) calculated as follows:

$$\tau_{avg} = \frac{\left(A_1 \times \tau_1^2\right) + \left(A_2 \times \tau_2^2\right)}{\left(A_1 \times \tau_1\right) + \left(A_2 \times \tau_2\right)}$$

Where A_i are the normalized pre-exponential factors of the bi-exponential function, τ_i are the decay times (See Table S4 and S5). However, for some materials we were able to achieve a good quality fit using a mono-exponential decay function. Using the τ_{avg}, we estimated the PL quenching efficiency.

Table S4: Parameters extracted by fitting the TRPL decays of the neat NFA and blend systems with the intensity-averaged lifetime (τ_{avg}) given, with acceptor excitation.

Systems	A_1	A_2	τ_1 (ps)	τ_2 (ps)	τ_{avg} (ps)
IT-4F	0.83	-	314.5	-	314.5
P3HT:IT-4F	1.08	0.08	3.38	15.84	6.69
Y6	0.46	0.44	521.2	1263.9	1040
P3HT:Y6	1.17	-	3.32	-	3.32
IEICO-4Cl	0.94	-	142.6	-	142.6
P3HT:IEICO-4Cl	0.44	0.57	4.23	18.65	16.5
IEICO-4F	0.95	-	163.2	-	163.2
P3HT:IEICO-4F	0.49	0.42	8.69	45.82	39.1
ICC6	0.36	0.60	97.6	385.5	347.2
P3HT:ICC6	0.46	0.45	10.20	46.04	39.4
BT-CIC	0.96	-	179	-	179
P3HT:BT-CIC	0.81	0.23	2.81	23.87	17.6
IEICO	0.87	-	285.9	-	285.9
P3HT:IEICO	0.56	0.44	11.91	55.54	46.1
ZY-4Cl	0.58	0.41	148.8	485.1	382.6
P3HT:ZY-4Cl	0.76	0.20	16.70	58.12	36.8
FBR	0.30	0.68	92.15	465.9	435.3
P3HT:FBR	0.54	0.40	14.22	73.28	61
IDT-2Br	0.96	-	390.4	-	390.4
P3HT:IDT-2Br	0.55	0.41	36.63	153.2	125.1
O-IDTBR	0.92	-	453.1	-	453.1
P3HT:O-IDTBR	0.511	0.44	77.3	160.3	130.8

Note: The sum of A_1 and A_2 should be equal to 1 because the amplitudes were normalized from the kinetics, and the difference is attributed to the background and noise errors.

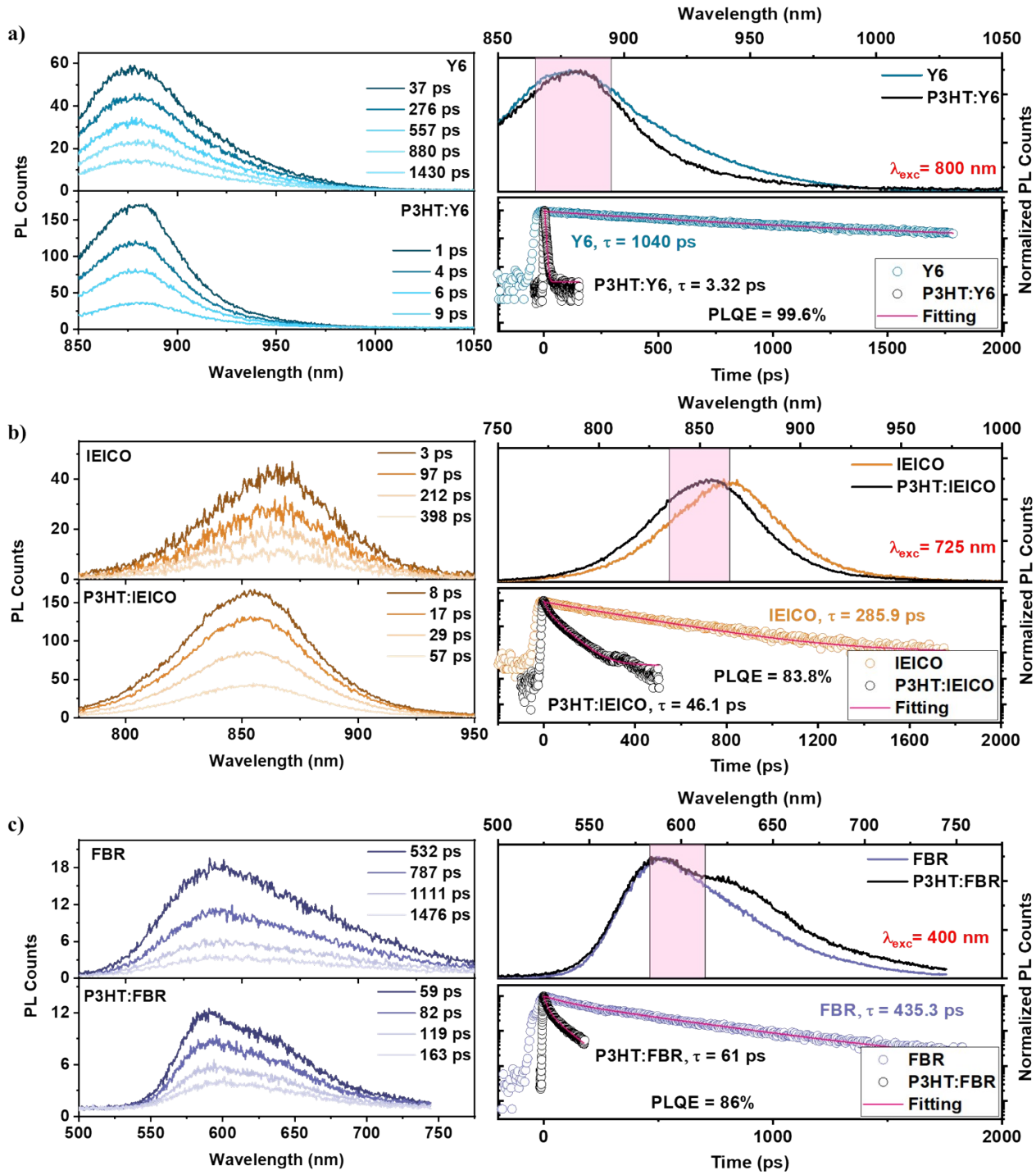

Fig. S13: TRPL measurements on neat NFAs and blends. The left hand side shows PL spectra at different times (time range ~ 0-2 ns for neat films and ~ 0-0.2 ns for blend films except for P3HT:IEICO the time range is ~ 0-0.6 ns) upon different optical excitations at 800 nm, 725 nm, and 400 nm respectively, of neat NFAs (top panel) and photoactive blends (bottom panel). The right column shows the normalized PL decays (bottom panel) tracked at the respective PL peak positions (shadowed in top panel) of the neat and blend thin films and fits to the data (solid pink lines) using bi-exponential functions.

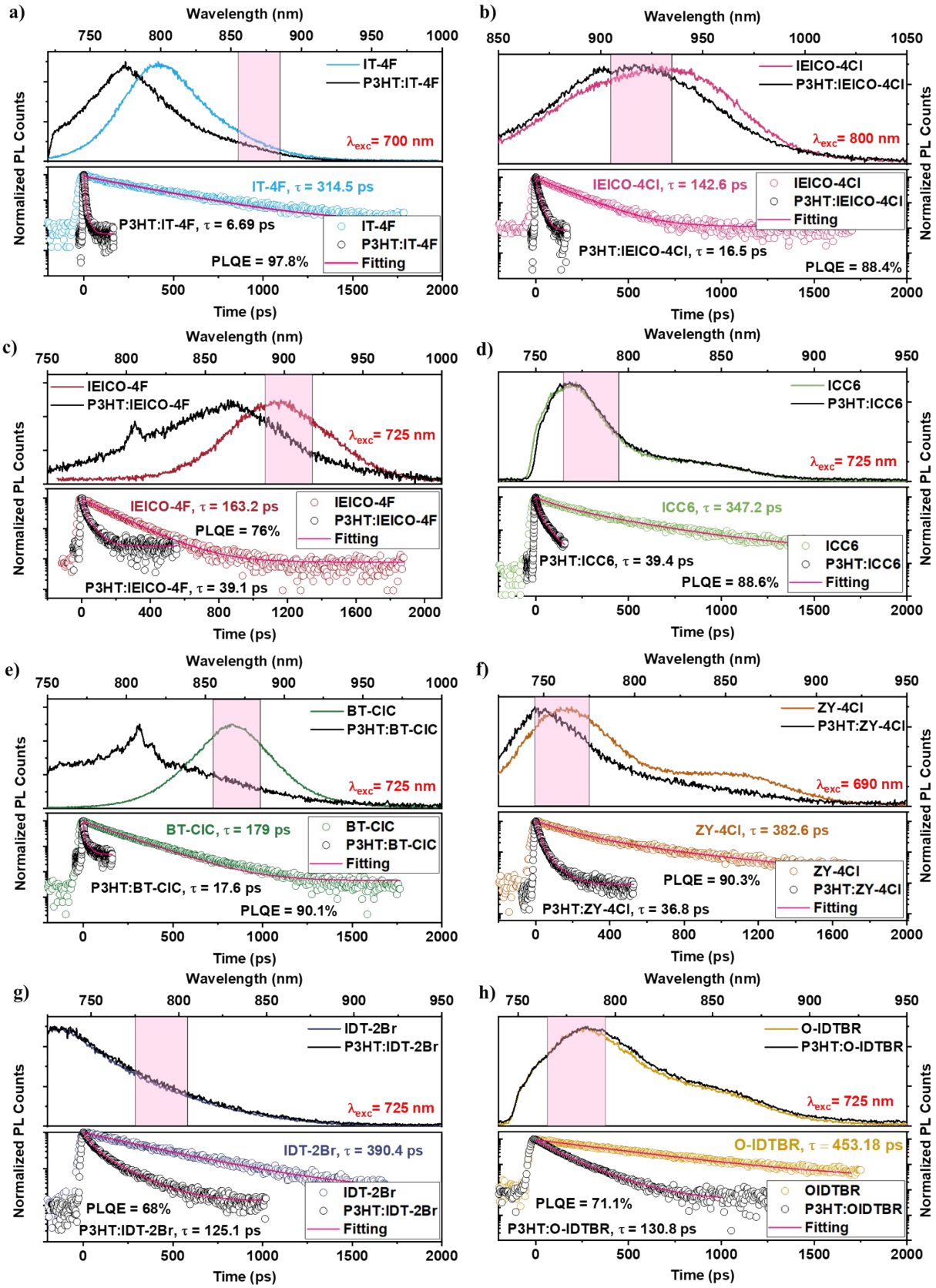

Fig. S14: Normalized PL decays (bottom panel) tracked at the respective PL peak positions when possible (shadowed in top panel) at different times (time range ~ 0-2 ns for neat films and ~ 0-0.2 ns for blend films except for P3HT:IT-4F and P3HT:ZY-4Cl the time range ~ 0-0.5 ns

and 0-0.6 ns, respectively) upon different optical excitations of neat NFA and blend thin films and fits to the data (solid pink lines) using bi-exponential functions.

Note: The time-averaged PL spectra and the spectrally-averaged PL kinetics are plotted in Figure S13. Figure S14 shows that the P3HT:IEICO-4F and P3HT:BT-CIC blends exhibited a broad PL spectrum, possibly indicating different molecular packing motifs in the blends. Here, the contribution of the NFA was found to be lower than expected.

Table S5: Parameters extracted by fitting the TRPL decays of the neat **P3HT** films and blend

Systems	A_1	A_2	τ_1 (ps)	τ_2 (ps)	τ_{avg} (ps)
P3HT for IT-4F	0.35	0.62	182.9	770.9	701.9
P3HT:IT-4F	0.82	0.13	2.71	9.59	5.2
P3HT for Y6	0.31	0.62	149.2	879.7	822.9
P3HT:Y6	1.00	-	8.91	-	8.9
P3HT for IEICO-4Cl*	0.29	0.62	160.2	886.2	828.1
P3HT:IEICO-4Cl	0.72	0.27	14.81	52.69	36.4
P3HT for IEICO-4F	0.31	0.63	127.2	727.2	679.1
P3HT:IEICO-4F	0.25	0.70	21.12	7.45	14.3
P3HT for ICC6	0.28	0.64	156.9	955.1	900.4
P3HT:ICC6	0.63	0.37	26.99	122.9	96.7
P3HT for BT-CIC	0.30	0.66	158	933.3	877.9
P3HT:BT-CIC	0.62	0.42	6.18	17.68	13.7
P3HT for IEICO*	0.29	0.62	160.2	886.2	828.1
P3HT:IEICO	0.25	0.73	53.43	16.08	36.1
P3HT for ZY-4Cl	0.35	0.63	164.9	785.4	721.2
P3HT:ZY-4Cl	0.57	0.43	58.77	253.8	208.4
P3HT for FBR	0.35	0.65	163.8	815.1	750.9
P3HT:FBR	0.99	0.08	32.05	176.2	77
P3HT for IDT-2Br	0.33	0.63	128.7	687.6	637
P3HT:IDT-2Br	0.79	0.21	27.34	115.5	74
P3HT for O-IDTBR	0.30	0.63	145	773.9	721.9
P3HT:O-IDTBR	0.63	0.39	41.2	166.2	130.5

films with the intensity-averaged lifetime (τ_{avg}) given, with donor excitation.

* The processing conditions for both blend films are the same, so we used the same P3HT film.

Note: The sum of A_1 and A_2 should be equal to 1 because the amplitudes were normalized from the kinetics, and the difference is attributed to the background and noise errors.

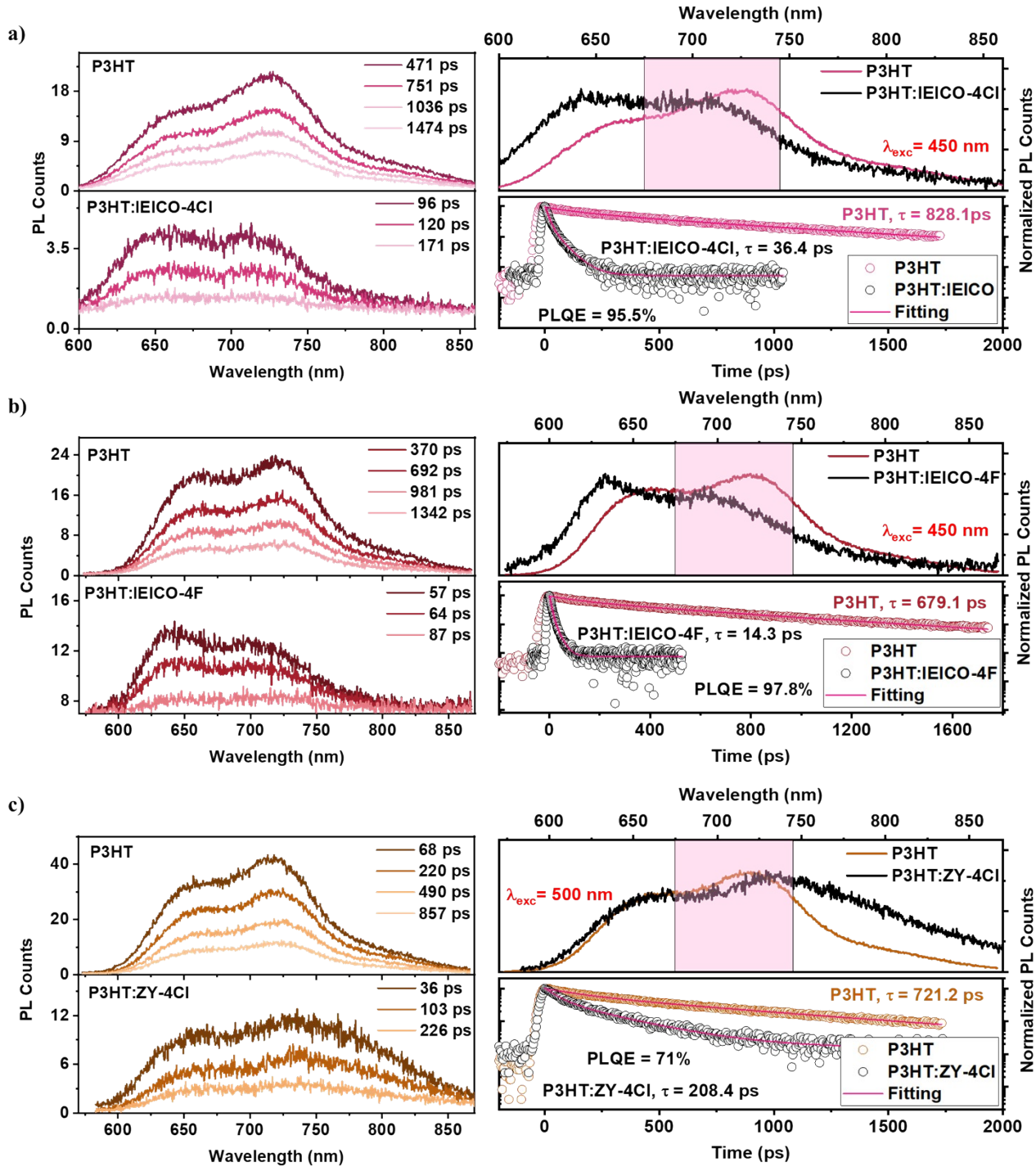

Fig. S15: TRPL measurements on neat P3HT films and blends. The left column shows PL spectra at different times (time range ~ 0-2 ns for neat and blend films except for P3HT:IEICO-4F the time range ~ 0-0.6 ns) upon different optical excitations at 450 nm and 500 nm respectively, of neat P3HT (top panel) and photoactive blends (bottom panel). The right column shows the normalized PL decays (bottom panel) tracked at the respective PL peak positions (shadowed in top panel) of the neat and blend thin films and fits to the data (solid pink lines) using bi-exponential functions.

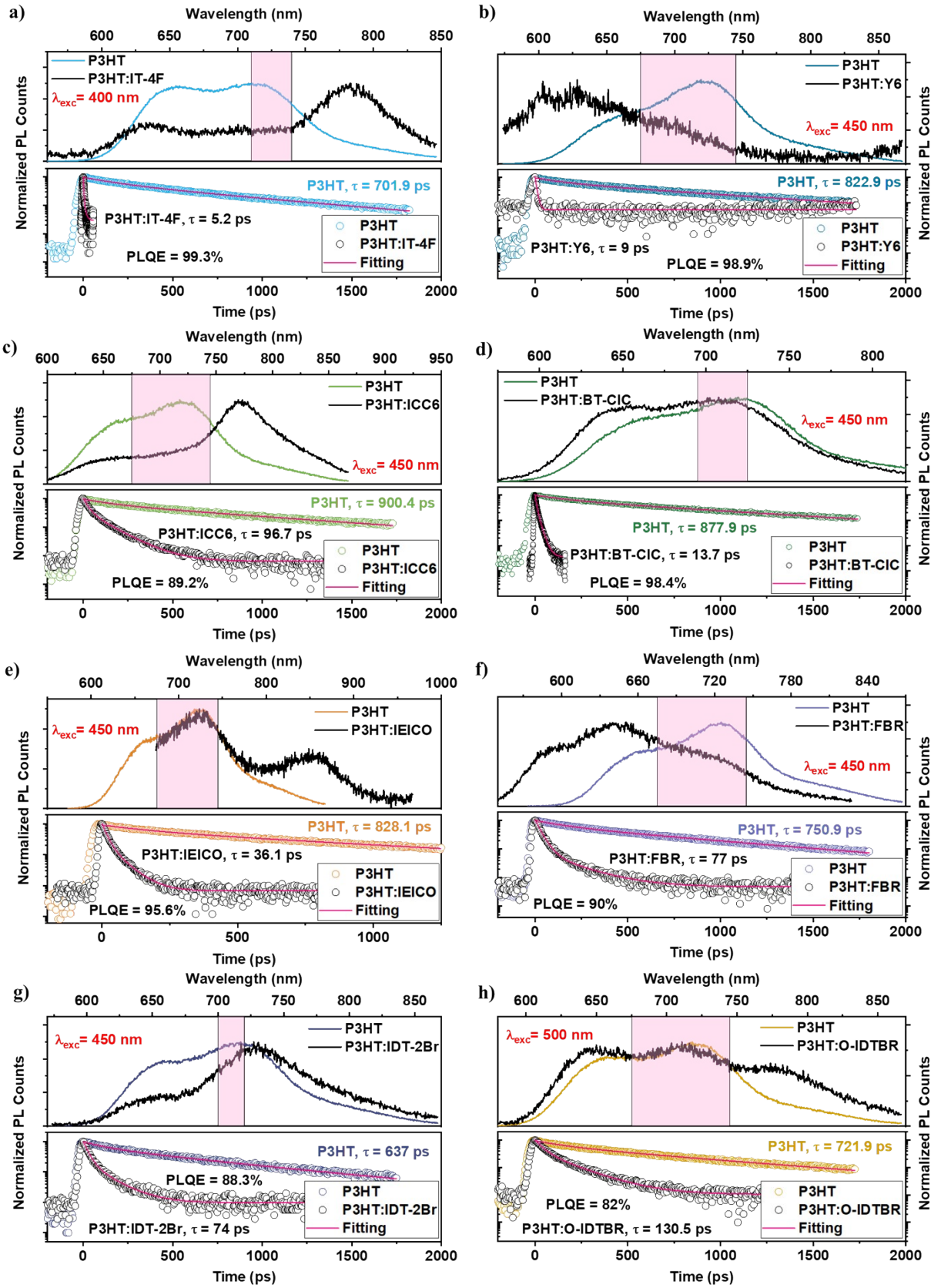

Fig. S16: Normalized PL decays (bottom panel) tracked at the respective PL peak positions (shadowed top panel) at different times (time range ~ 0-2 ns for neat and blend films except for P3HT:IT-4F, P3HT:BT-CIC, P3HT:IEICO the time range ~ 0-0.06 ns, 0-0.2 ns, and 0-0.5 ns, respectively) upon different optical excitations of neat P3HT and blend thin films and fit to the data (solid pink lines) using bi-exponential functions.

We examined the photoluminescence decays of neat P3HT films prepared with different processing conditions of the representative NFAs, and of the corresponding blends. Our focus was to gain a better understanding of the PLQE and the formation of charge-transfer states. Figure S15 shows the TRPL measurement on P3HT films and blends selectively photoexcited at 400 nm or 500 nm to limit photoexcitation of the NFA as much as possible. The time-resolved emission spectra (TRES) of neat P3HT, as well as P3HT:IEICO-4Cl, P3HT:IEICO-4F, and P3HT:ZY-4Cl blends measured at different times are shown in Figure S15 (left column), while the TRES of the other systems following donor photoexcitation can be found in Figure S16. The PL spectra of neat P3HT films show the well-known broad emission with two distinct bands at 650 nm and 730 nm. These two peaks originate from the emission of semi-crystalline regions of P3HT, precisely the 0-0 and 0-1 transitions of H-aggregates.[10–12] Moreover, we observe spectral shifts between the PL of neat P3HT films prepared with different solvents and processing conditions. The PL spectra of the blend films observed after donor photoexcitation are red-shifted in most of the systems (Figure S15 and S16), indicating partial photoexcitation of both the acceptor and the donor or the presence of energy transfer. The parameters extracted from fits to the TRPL decays of the neat P3HT ($\tau_{neat(P3HT)}$) films and the blends are shown in Table S5.

Table S6: The intensity-averaged PL lifetimes and quenching efficiency. For neat NFAs $\tau_{neat(NFA)}$, neat P3HT $\tau_{neat(P3HT)}$, and τ_{blends} of the photoactive blends along with the estimated PLQE.

Systems	Acceptor Excitation		Donor Excitation	
	$\tau_{neat(NFA)}$ and τ_{blend} (ps)	PLQE (%)	$\tau_{neat(P3HT)}$ and τ_{blend} (ps)	PLQE (%)
IT-4F, P3HT	314.5		701.9	
P3HT:IT-4F	6.69	97.8	5.2	99.3
Y6, P3HT	1040		822.9	
P3HT:Y6	3.32	99.6	8.9	98.9
IEICO-4Cl, P3HT	142.6		828.1	
P3HT:IEICO-4Cl	16.5	88.4	36.4	95.5
IEICO-4F, P3HT	163.2		679.1	
P3HT:IEICO-4F	39.1	76	14.3	97.8
ICC6, P3HT	347.2		900.4	
P3HT:ICC6	39.4	88.6	96.7	89.2
BT-CIC, P3HT	179		877.9	
P3HT:BT-CIC	17.6	90.1	13.7	98.4
IEICO, P3HT	285.9		828.1	
P3HT:IEICO	46.1	83.8	36.1	95.6
ZY-4Cl, P3HT	382.6		721.2	
P3HT:ZY-4Cl	36.8	90.3	208.4	71
FBR, P3HT	435.3		750.9	
P3HT:FBR	61	86	77	90
IDT-2Br, P3HT	390.4		637	
P3HT:IDT-2Br	125.1	68	74	88.3
O-IDTBR, P3HT	453.1		721.9	
P3HT:O-IDTBR	130.8	71.1	130.5	82

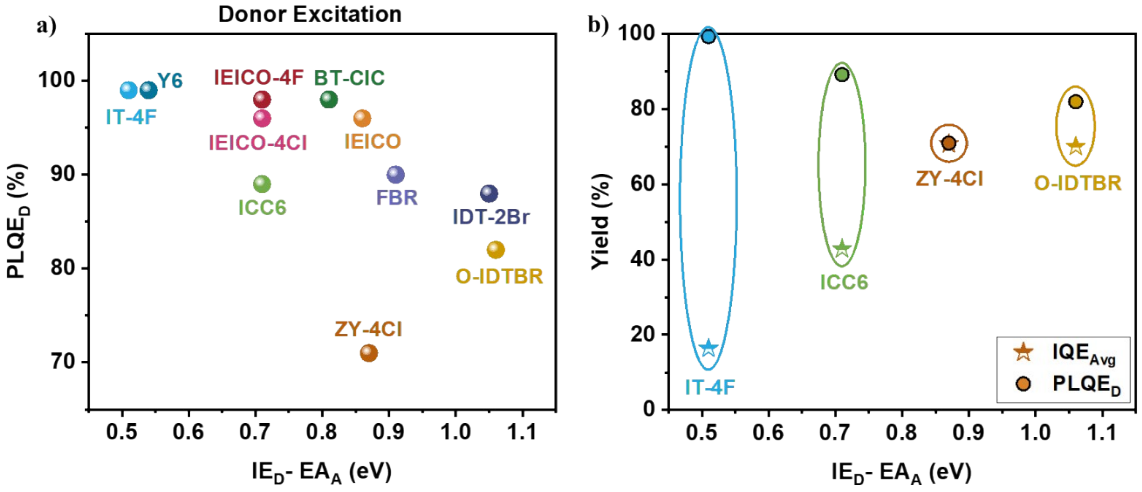

Fig. S17: a) Photoluminescence Quenching Efficiency at donor excitation ($PLQE_D$) versus diagonal bandgap. b) IQE_{Avg} (stars) and $PLQE_D$ (circles) as a function of diagonal bandgap.

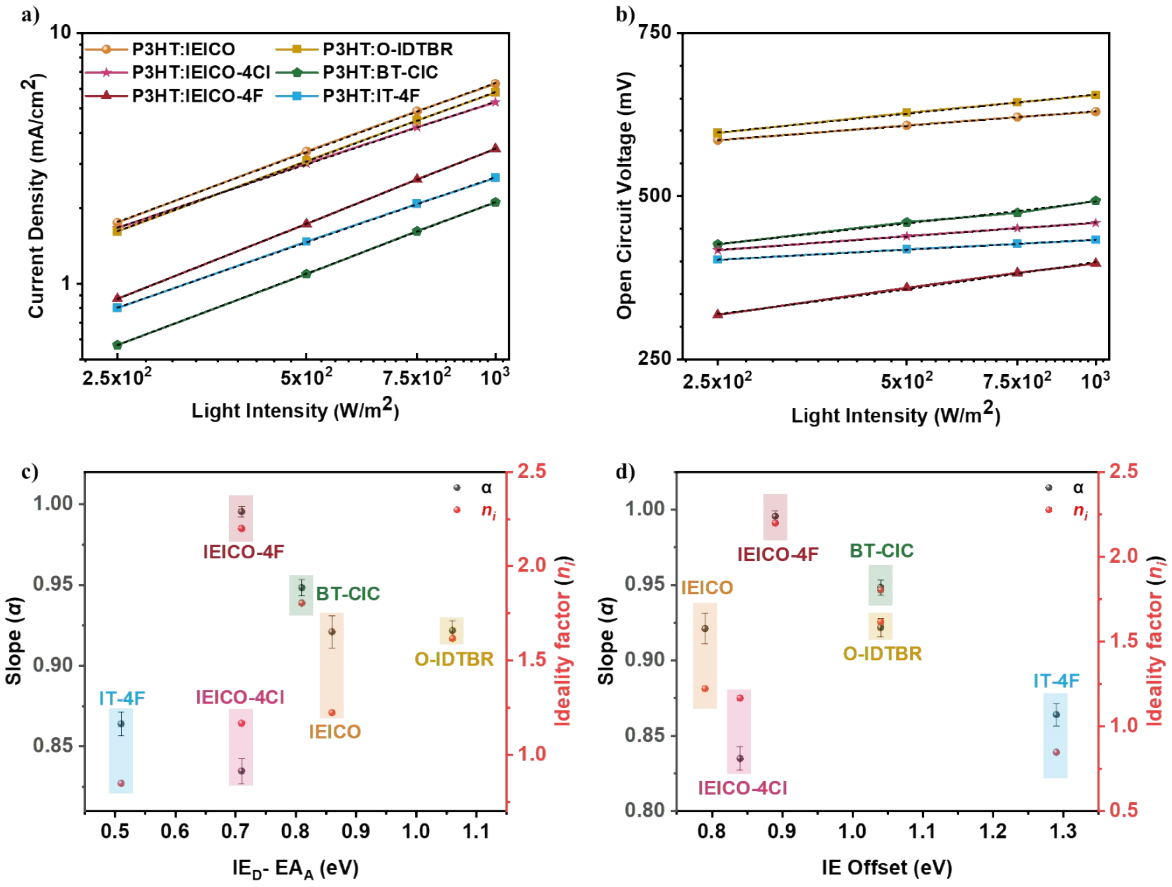

PAIOS

Fig. S18: PAIOS measurements showing, a) current density and b) open-circuit voltage against light intensity, black dashed lines indicate the linear fit to all the data points. The extracted slope

(α) from log-log J_{SC} versus light intensity plot, and calculated ideality factor (n_i) determined from semi-log V_{OC} versus light intensity plot of the representative systems against c) diagonal bandgap, and d) IE offset.

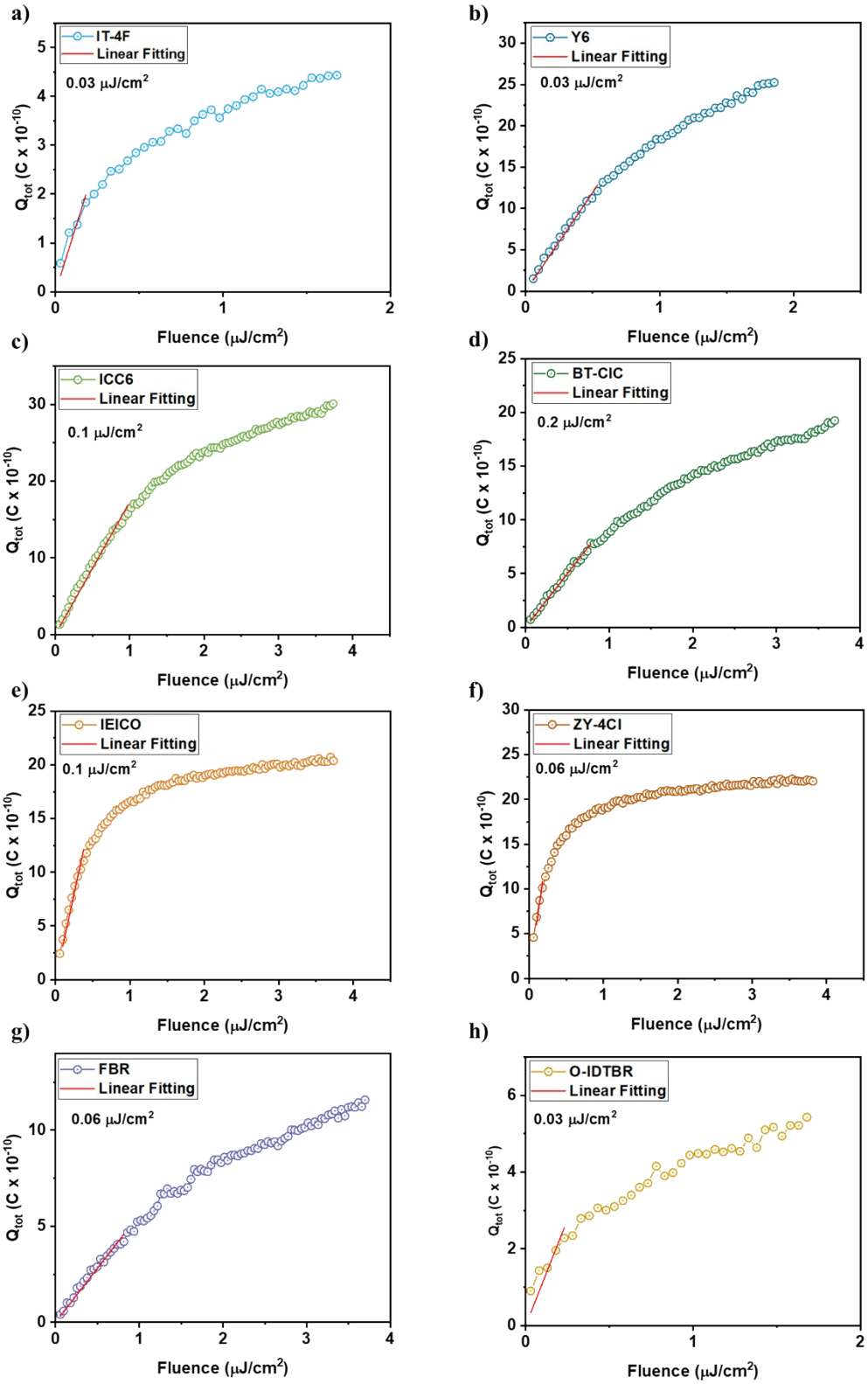

Time-Delayed Collection Field (TDCF)

Fig. S19: Total extracted charges versus laser fluence for P3HT:NFAs based devices. Excited at 532 nm with 50 ns delay time, pre-bias at V_{OC}, and collection bias equal to -4V. A range of

low pulse fluences were used (0.03 μJ/cm^2 – 0.2 μJ/cm^2), for P3HT:BT-CIC we used 0.2 μJ/cm^2 which is the highest fluence among the systems to improve the signal-to-noise ratio.

Figure S19 shows that the photoexcitation was in the linear regime, working in the linear regime of Q vs. I is needed to ensure minimal losses due to non-geminate recombination of photogenerated carriers. We also tried to minimize the recombination of photogenerated carriers with dark (injected) carriers by using the higher part of the linear region to keep the density of photogenerated carriers large compared to the density of (injected) dark carriers.[13] Furthermore, a strong extraction bias (-4 V) was applied to expedite the carrier extraction process prior to the onset of non-geminate recombination. It is important to ensure extraction as early as possible before non-geminate recombination takes effect, however, a short delay of 10 ns between photo-generation and extraction is unavoidable due to instrument limitations. Note: see the transient absorption (after Table S7) for details of the fluence calculation.

Q_{tot} was determined by integrating the photocurrent transients obtained when applying a strong charge-collection field. All devices were subjected to pre-biases (V_{pre}) ranging from -1V to 1V during photoexcitation with a sub-ns laser pulse followed by a short (instrument-limited) delay of 10 ns between photoexcitation and charge collection pulses. The photoexcitation was conducted at 532 nm at low pulse fluences of 0.03 μJ/cm^2 – 0.2 μJ/cm^2, i.e., under conditions that largely avoid non-geminate charge recombination in the first 10 ns.

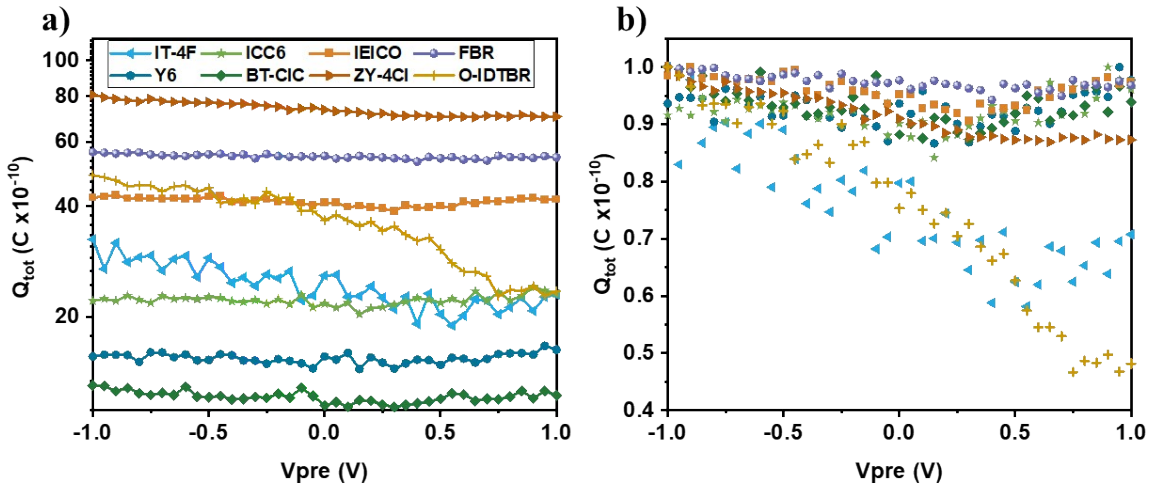

Fig. S20: a) Total extracted charge (Q_{tot}). b) Normalized Q_{tot} at -1V as a function of pre-bias (V_{pre}). Photo-excitation at 532 nm with 50 ns delay time, collection bias equal to -4V, and laser pulse fluence ranged from 0.03 to 0.2 μJ/cm^2.

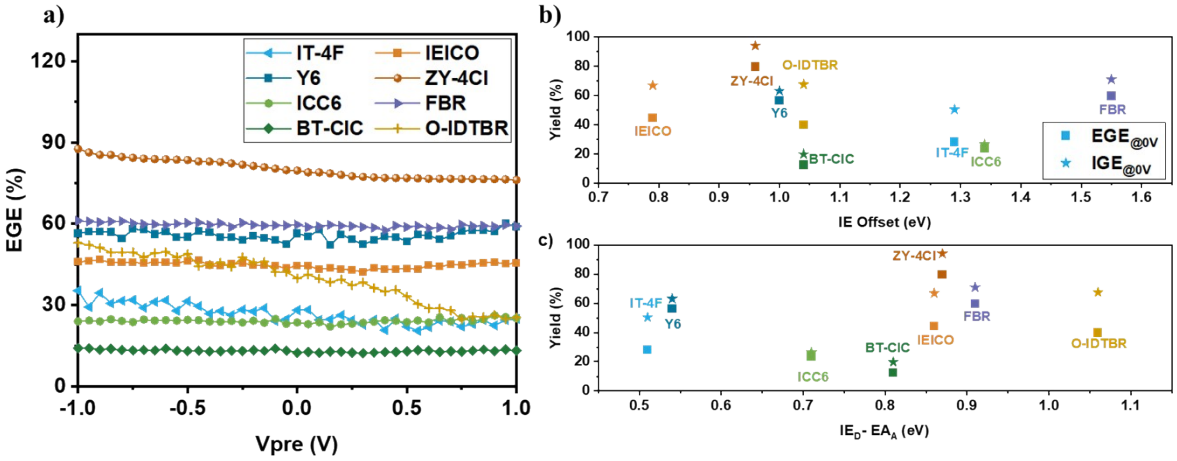

Fig. S21: a) External generation efficiency (EGE_{TDCF}) as a function of pre-bias (V_{pre}). external generation efficiency ($EGE_{@0V}$) (squares) at 0 V and internal generation efficiency ($IGE_{@0V}$) (stars) at 0 V against b) IE offset, and c) diagonal bandgap IE_D-EA_A.

Transient Absorption Spectroscopy (TAS)

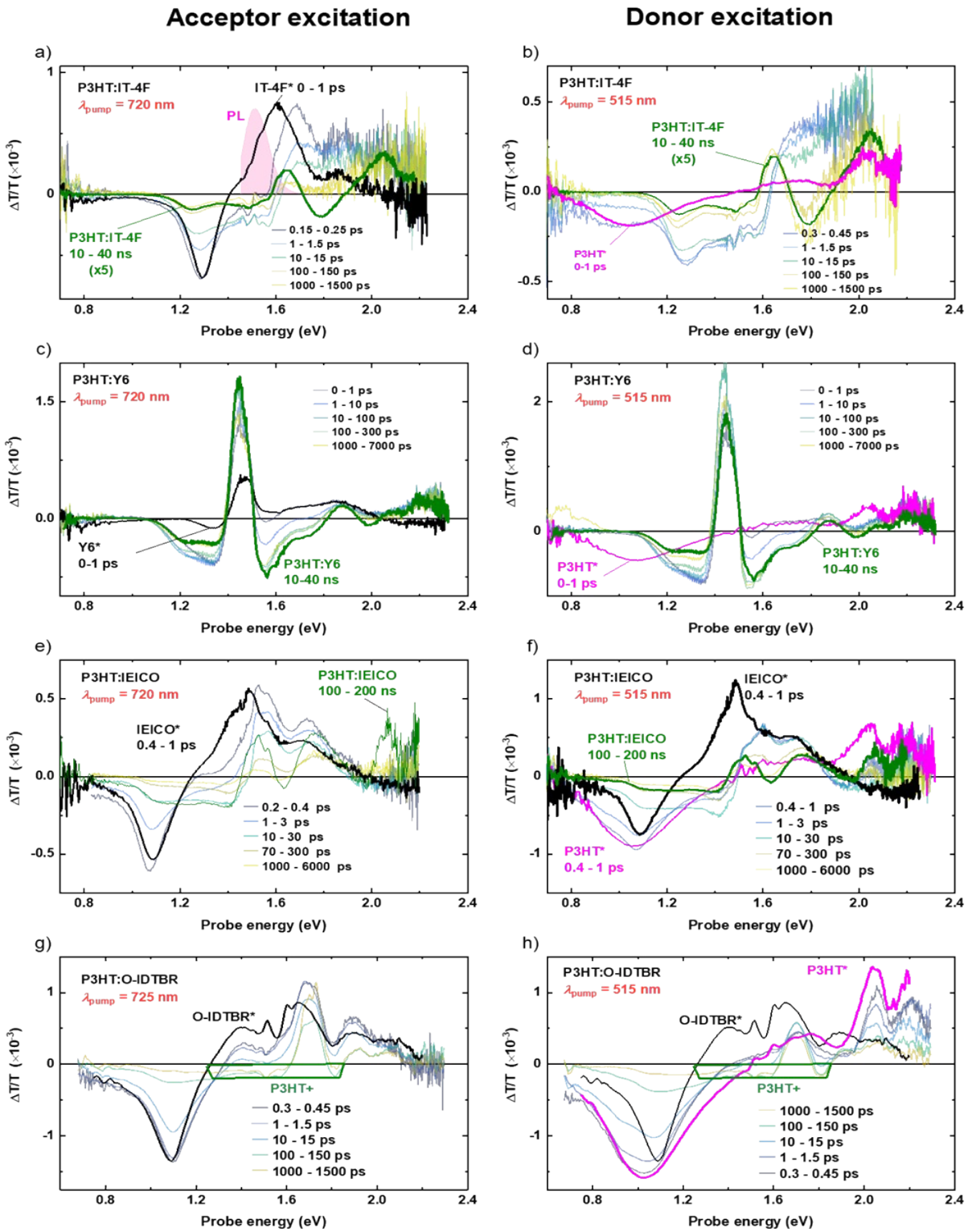

Fig. S22: Features identification on low fluence spectra: the curves with transparency show the excited species spectra of blend films at various delays following the initial excitation of the acceptor (left column) and P3HT (right columns), respectively. Fluences used:

Upon acceptor photoexcitation (left panels on Fig. S22), the initial (sub-picosecond) spectra are dominated by acceptor exciton-induced signatures, with a small contribution from charges generated ultrafast. More precisely, the sub-picosecond blend spectra are almost identical to the acceptor exciton-induced spectra (black lines) obtained from TA on pristine NFA films. However, the positive features (photo-bleach and stimulated emission) differ slightly from that of the pristine films, possibly due to the early generation of charges: (i) a slight photobleach signal can be seen in the P3HT absorption region (>2 eV) and (ii) the stimulated emission of the excitons (in the PL region, as highlighted in panel a) for the case of IT-4F) is weaker (P3HT:O-IDTBR) or even absent (P3HT:IT-4F and P3HT:IEICO), most likely due to the early presence of charges whose photo-induced absorption in that region compensates the positive signal from stimulated emission.

Upon donor photoexcitation (right panels in Fig. S22), both P3HT (compare with the pink reference measured in pristine P3HT films) and acceptor exciton-induced signatures can be seen in different proportions depending on the material systems: P3HT:IT-4F exhibits clear P3HT* signature and almost no IT-4F*), P3HT:Y6 shows no P3HT* contribution can be detected, due either to ultrafast energy transfer to Y6 or ultrafast charge generation, or a combination of both, finally P3HT:IEICO and P3HT:O-IDTBR exhibit both excitons' signature.

Note that the pristine P3HT spectra presented in Fig. S22 are not the same for all the samples, as we prepared several P3HT films for conditions matching the blends optimal conditions, which are not the same for all the blends (See Table S2).

Eventually all the systems exhibit different spectral signatures in the ps to ns timescale, depending on the systems, whose shape does not evolve further within several tens of nanoseconds (see green solid curves in Fig. S22) and is thus attributed to charges. As highlighted in panel g) and h), this signature includes the well know $P3HT^+$ polaron spectra from 1.24 eV to roughly 1.8 eV,[14,15] together with the photobleach of the acceptors and some photoinduced absorption at lower energy (except for Y6 were the photoinduced absorption appears on both sides of the photobleach) that we attribute to the NFA negative polarons.

Focusing on spectra obtained at low fluences, to limit second order effects, we were able to observe isosbestic points (Fig. S23) in all systems except P3HT:Y6 upon acceptor excitation. At those energies/wavelengths, excitons and charges exhibit the same cross section; as a result, charge transfer occurs without modifying the signal amplitude. Those points can thus be used to monitor the overall evolution of the excitation density independently of whether the excited states are excitons or charges.

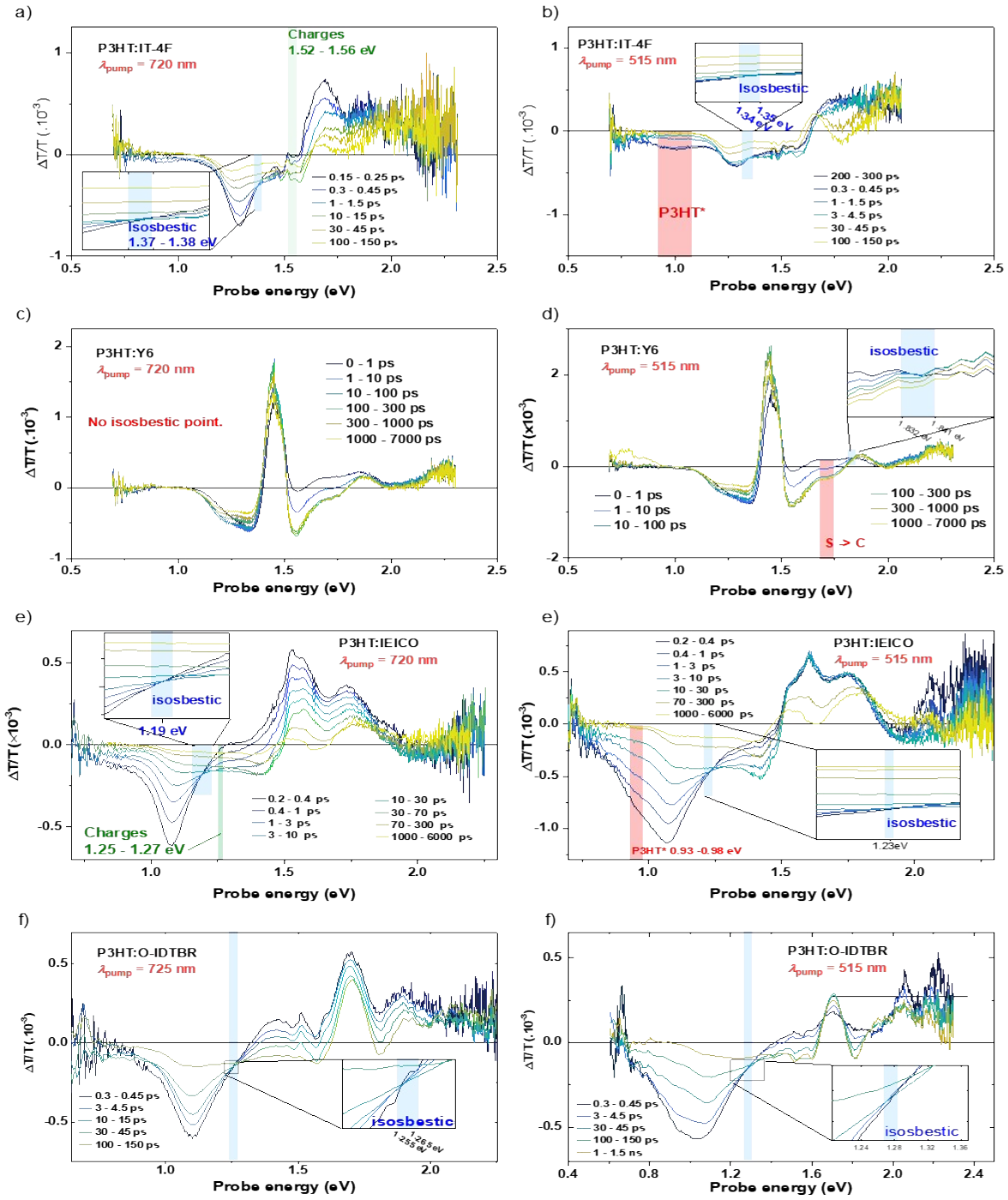

Fig. S23: Isosbestic points and exciton / charge features.

We used the dynamics of those isosbestic points to evaluate how much of the excitation is still present in the film at the conclusion of the exciton-to-charge conversion. We approximated this point in time as the point at which all excitons had disappeared (P3HT:IT-4F, P3HT:Y6 and P3HT:IEICO under P3HT excitation) or when we could not find a region where only excitons absorbed, as the point where the charge signal was maximal (P3HT:IT-4F and P3HT:IEICO under NFA excitation). In the case of P3HT:O-IDTBR, the two excitons as well as the charge contribution were separated using the Matlab multivariate curve resolutions tool developed by Jaumot, de Juan and Tauler (see Fig. S25).[16–19]

Note1: the isosbestic point used for P3HT:Y6 is not strictly isosbestic as a slight spectral shift is observed during charge generation, possibly due to a contribution from electroabsorption. Hence, the estimate is only an approximation of the charge generation efficiency.

Note2: for the cases of P3HT:Y6 upon donor excitation, P3HT:IEICO upon acceptor excitation, and P3HT:IT-4F upon acceptor excitation, we did not identify a region where only excitons or only charges absorbed, as such a region did not exist. We monitored instead a spectral region where excitons have a positive contribution and charges a negative contribution. The time point chosen for the end of charge generation is thus the point at which the signal is the most negative. In details for P3HT:IEICO and P3HT:IT-4F under acceptor excitation, exciton signal and charge signal almost cancel each other at initial time resulting in an initial signal close to 0 (Fig. S25a) and S25e)). We draw the reader's attention to the fact that this is not strictly due to an absence of charges, but to a charge signal almost exactly compensating the exciton signal at that time. For P3HT:Y6 under donor excitation the signals do not cancel out, and the signal intensities were normalized from 0 to 1, with 0 at the most negative signal and 1 at the most positive signal.

In the case of P3HT:O-IDTBR, charge generation and energy transfer were somewhat slower than in the other systems, such that P3HT excitons, O-IDTBR excitons, charges, and even triplets for the longer time range, had a strong temporal overlap, in addition to their spectral overlap. Hence, we used multivariate curve resolution to separate those four contributions.

The spectral shape of excitons was obtained from TAS on pristine materials (same as presented in Fig. S22). The spectral shape of charges was obtained from the long delay spectra (ns to microseconds) upon low excitation density. Indeed, at low fluences, spectra were found to not evolve over time, which was attributed to charges mostly recombining directly to the ground state. On the other hand, for larger excitation density, a strong spectral evolution was found which we attribute to the formation of triplets upon the larger recombination rate obtained for

those fluences. Finally, the triplet spectra were found by the MCR algorithm as the fluence and time dependent (the intensity is dependent, not the spectral shape) difference between the previously given charge spectra and the experimental signal obtained in ns-µs time scale. A limited freedom was left for the algorithm to adapt the components' spectra (see Fig. S24d-f) to slight experimental variations. Finally, the regions of intense pump scattering or excessively noisy signal had to be excluded from the fit in the case of O-IDTBR excitation, where the excitation is done in a weak absorption region (to be sure to exclude P3HT) resulting in weak signals. Note that this is an issue only with O-IDTBR due to its bandgap closer to that of P3HT than in those of the other NFAs.

Table S7: Excitation wavelength (λ_{Exc}), fluences and the corresponding absorbed photon densities $N_{0,Abs}$, and absorbed fluence used in TAS.

Systems and film thicknesses	**Excitation (λ_{Exc}) and absorptance $(\%A)$**	**Fluence (µJ/cm²)**	**Absorbed Fluence (µJ/cm²)**	**$N_{0,Abs}$ (cm^{-3})**
P3HT:IT-4F 93 nm	515 nm %A = 46 %	1.6	0.74	2.1×10^{17}
		3.2	1.47	4.1×10^{17}
		7.3	3.4	9.4×10^{17}
		14.5	6.7	1.86×10^{18}
		14.8	6.8	1.9×10^{18}
		21	9.7	2.7×10^{18}
		29	13.3	3.7×10^{18}
	720 nm %A = 52 %	0.62	0.322	1.3×10^{17}
		2.5	1.3	5.1×10^{17}
		4.9	2.5	9.9×10^{17}
		5.0	2.6	1×10^{18}
		7.0	3.6	1.4×10^{18}
		10.3	5.4	2.1×10^{18}
P3HT:Y6 120 nm	515 nm %A = 54 %	1.26	0.68	1.47×10^{17}
		2.8	1.51	3.3×10^{17}
		5.7	3.1	6.6×10^{17}
		12	6.5	1.4×10^{18}
		12.3	6.6	1.43×10^{18}
		16.7	9	9×10^{18}
		26	14	3×10^{18}
	720 nm %A = 56 %	0.81	0.45	1.37×10^{17}
		1.73	0.97	2.9×10^{17}
		3.5	1.96	5.9×10^{17}
		6.78	3.8	1.15×10^{18}
		6.83	3.82	1.16×10^{18}
		11.6	6.5	1.96×10^{18}

Systems and film thicknesses	Excitation (λ_{Exc}) and absorptance (%A)	Fluence (µJ/cm²)	Absorbed Fluence (µJ/cm²)	$N_{0,Abs}$ (cm^{-3})
P3HT:IEICO 196 nm	515 nm %A = 68 %	1.32	0.9	1.2×10^{17}
		2.7	1.84	2.4×10^{17}
		6.5	4.4	5.8×10^{17}
		12.9	8.8	1.16×10^{18}
		17.7	12	1.59×10^{18}
		26	17.7	2.34×10^{18}
	720 nm %A = 78 %	0.71	0.55	1.02×10^{17}
		1.3	1.01	1.87×10^{17}
		3.1	2.4	4.5×10^{17}
		5.8	4.5	8.4×10^{17}
		8.1	6.3	1.17×10^{18}
		11.2	8.7	1.61×10^{18}
P3HT:O-IDTBR 80 nm	515 nm %A = 48 %	1.96	0.94	3.1×10^{17}
		4.7	2.3	7.3×10^{17}
		11.1	5.3	1.72×10^{18}
		17.6	8.4	2.7×10^{18}
		33	16	5.1×10^{18}
	725 nm %A = 36 %	1.54	0.55	2.5×10^{17}
		3	1.08	4.9×10^{17}
		6.4	2.3	1.05×10^{18}
		9.9	3.6	1.63×10^{18}
		18	6.5	3×10^{18}

Notes:

Incident fluences: To assess those excitation densities, the pump beam profile was measured with a Coherent beam profiler (LaserCam-HR II) at the point where the pump and probe beams overlap. We obtained 2D Gaussian beam profiles with similar but not identical diameters along the two axes. The fluences mentioned in that table are the peak fluences corresponding to the top of the Gaussian as the beams were aligned to overlap in this position (the probe beam has a much smaller diameter, between 10 and 100 times, than the pump). This peak fluence is double the one obtained by dividing the laser pulse energy by the beam surface area calculated using the $1/e^2$ Gaussian beam radius.

The pulse energy was obtained by dividing the beam power by the repetition rate.

Note: in TDCF the excitation beam has an almost square profile (a very broad Gaussian where only the very broad peak maximum is kept, while the rest is cut by an iris). The fluence is thus simply the pulse energy divided by the beam diameter.

Absorbed fluences: The absorptance was calculated by simulating the film in vacuum using the refractive indexes and extinction coefficients from ellipsometry already used to calculate the IQE (see Fig. S3).

Absorbed photon density: The absorbed photon density was obtained by dividing the absorbed fluence by the energy of a single photon, and the thickness of the sample. It is thus an average excitation density through the sample thickness (see Fig. S9).

We note that using the exciton decay as a probe for the completion of charge transfer can lead to an underestimation of φ_{CT} as some of the charges may already have recombined by the time the excitons have vanished (especially in P3HT:O-IDTBR due to the long exciton lifetime). Likewise, using the buildup of charges to probe the charge transfer may overestimate the charge transfer efficiency, as some of the signal of the excited states may originate from excitons. Here, we used the exciton decay for the P3HT:NFA blends upon donor excitation plus P3HT:O-IDTBR upon O-IDTBR excitation, and the charge formation for P3HT:IEICO and P3HT:IT-4F upon acceptor excitation. Overall, we found a rather good agreement between the charge transfer efficiency estimated from charge formation and from exciton decays, suggesting a rather small over- / under- estimation of φ_{CT}.

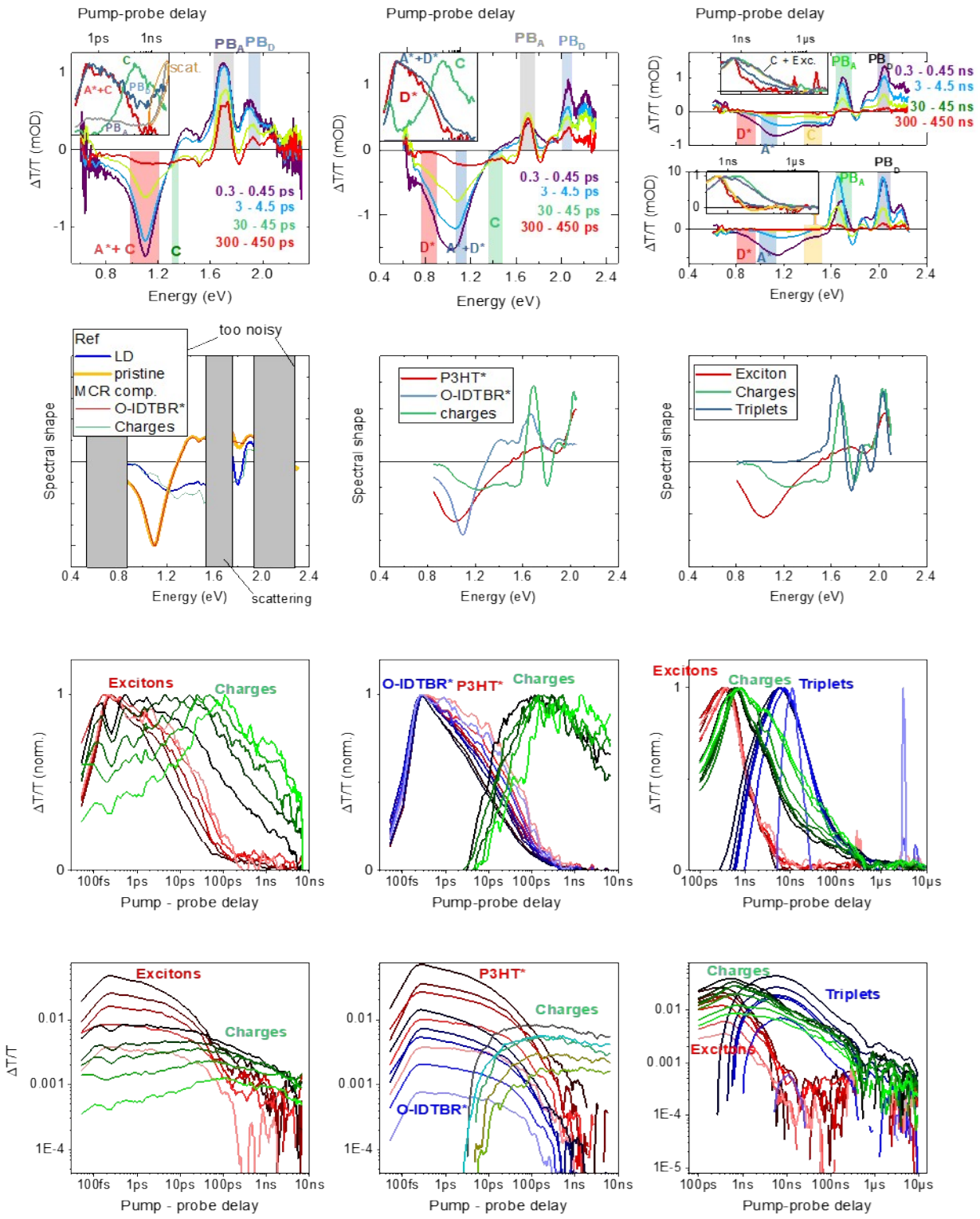

Fig. S24: Multivariate curve resolution on P3HT:O-IDTBR.

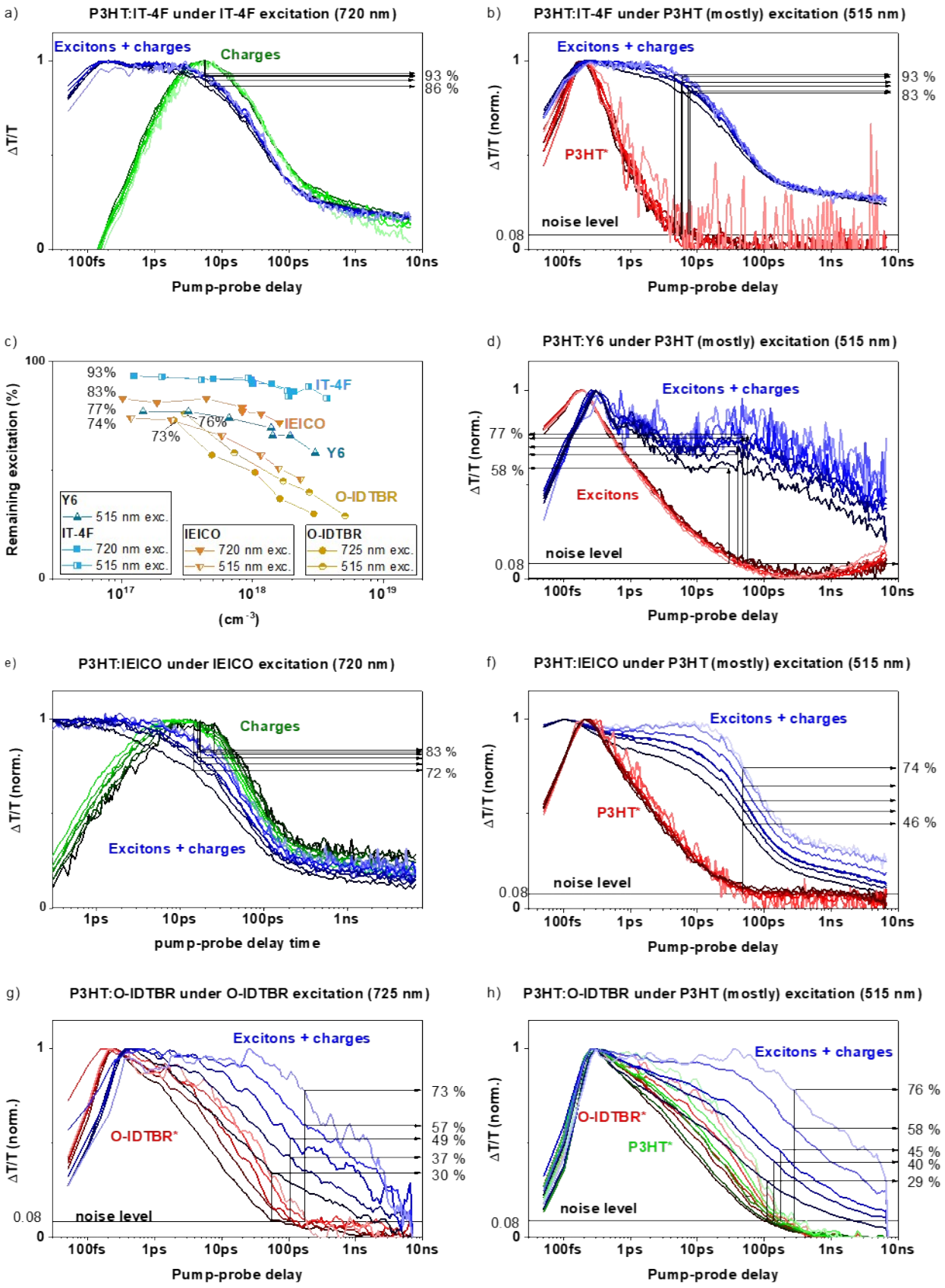

Fig. S25: Fluence dependence of charge generation and recombination.

Delay dependent Time-Delayed Collection Field (TDCF)

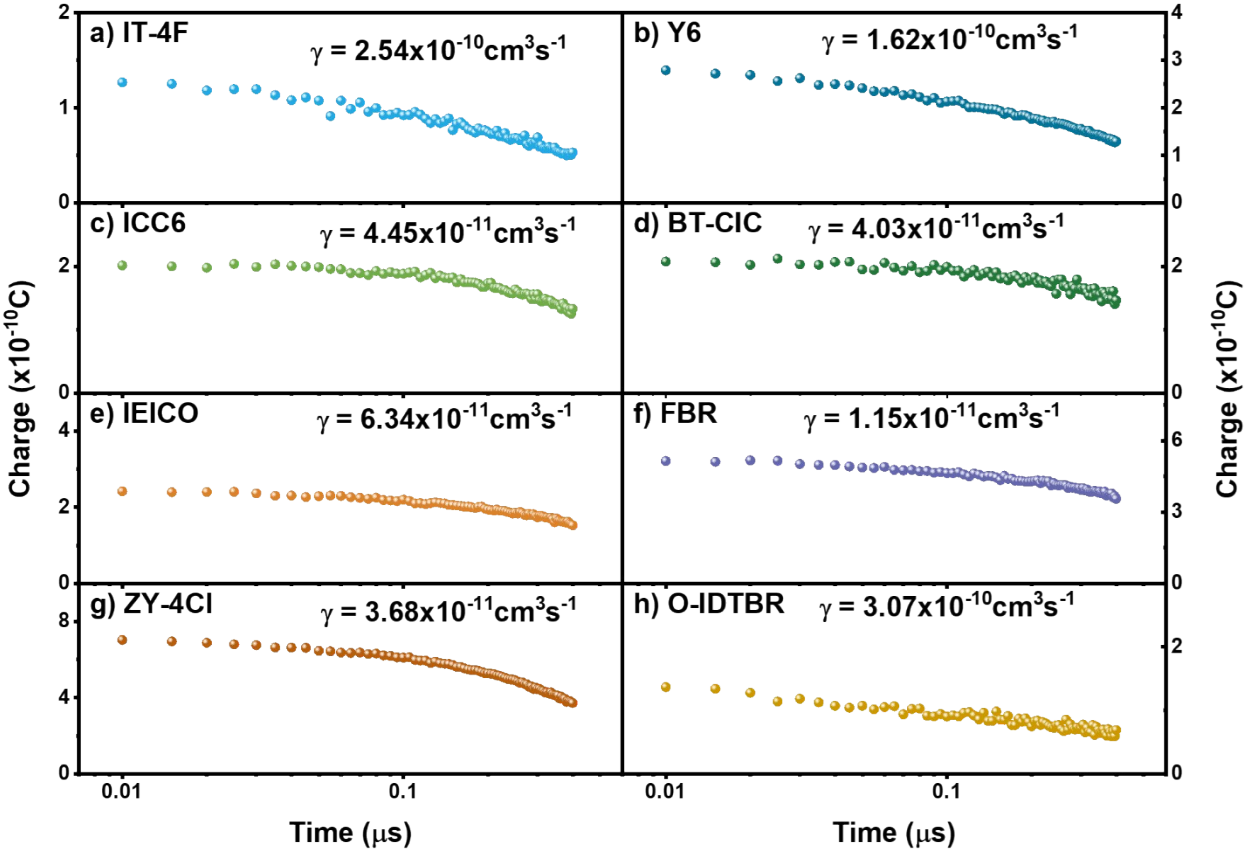

Fig. S26: (a-h) Fits of the extracted Q_{coll} charge as a function of delay time yields the bi-molecular recombination rate (γ).

Charge Carrier Mobility

Electron (μ_e) and hole (μ_h) mobilities in P3HT:NFA devices were determined using space-charge-limited current (SCLC) method by fitting the dark current of the *J-V* curves using Mott-Gurney relationship[20]:

$$J = \frac{9}{8}\varepsilon_0\varepsilon_r\mu\frac{v^2}{L^3}$$

Where, J is the current density, ε_0 is the vacuum permittivity = 8.85419×10^{-12} $(F\,m^{-1})$, ε_r is the dielectric constant of the polymeric materials ~ 3, μ is the charge carrier mobility, v is the potential across the device, and L is the thickness of the active layer.

Hole-only device architecture: ITO/MoO_X/P3HT:NFAs/MoO_X/Ag

Electron-only device architecture: ITO/ZnO/P3HT:NFAs/ZnO/Ag

Table S8: Estimated electron (μ_e) and hole (μ_h) mobility in P3HT:NFA devices.

System	μ_e	μ_h
	$(\times 10^{-4}\,cm^2V^{-1}S^{-1})$	
P3HT:IT-4F	1.27	0.93
P3HT:IEICO-4Cl	5.89	3.31
P3HT:IEICO-4F	1.89	2.00
P3HT:BT-CIC	5.68	7.83
P3HT:IEICO	0.70	2.79
P3HT:FBR[21]	0.018	1.4
P3HT:ZY-4Cl[22]	0.36	0.70
P3HT:O-IDTBR	3.36	3.24

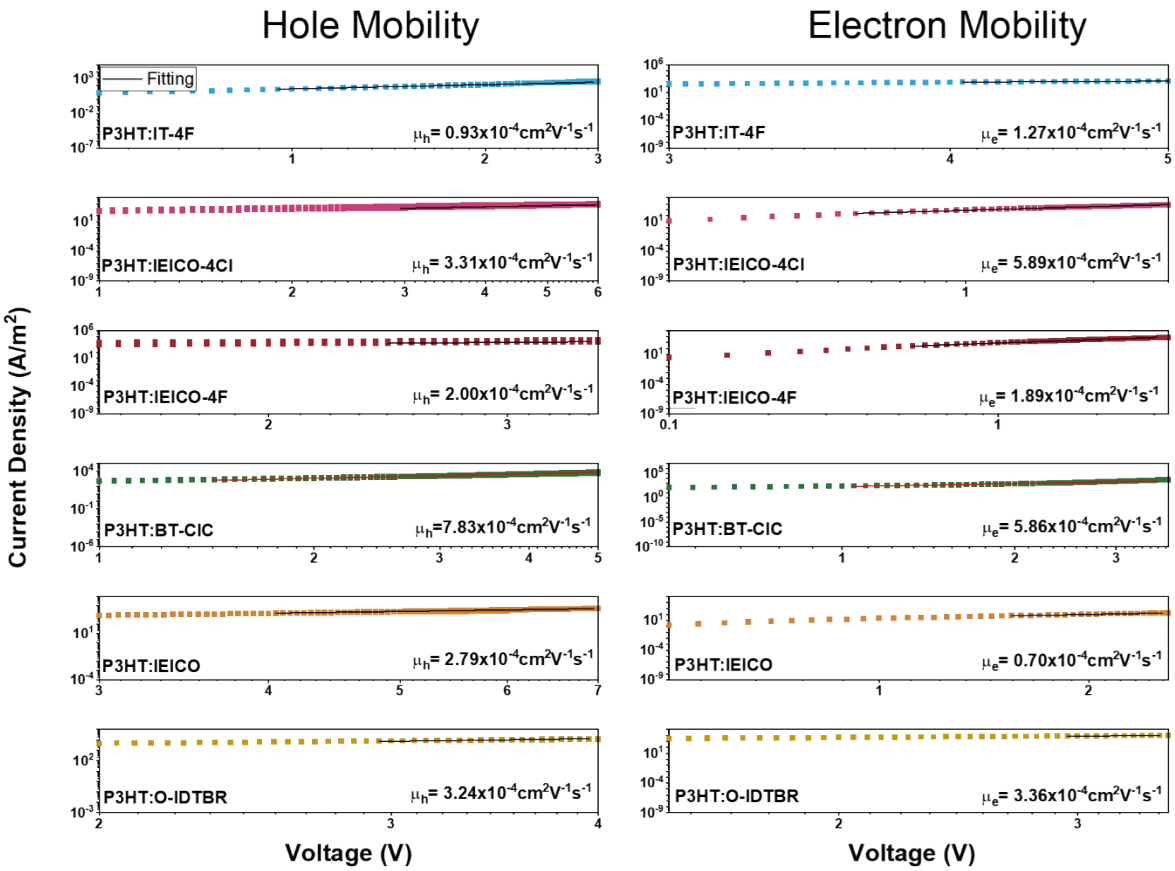

Fig. S27: Hole and electron mobility measered by SCLC method for P3HT:NFAs based blends.

Extraction versus Recombination

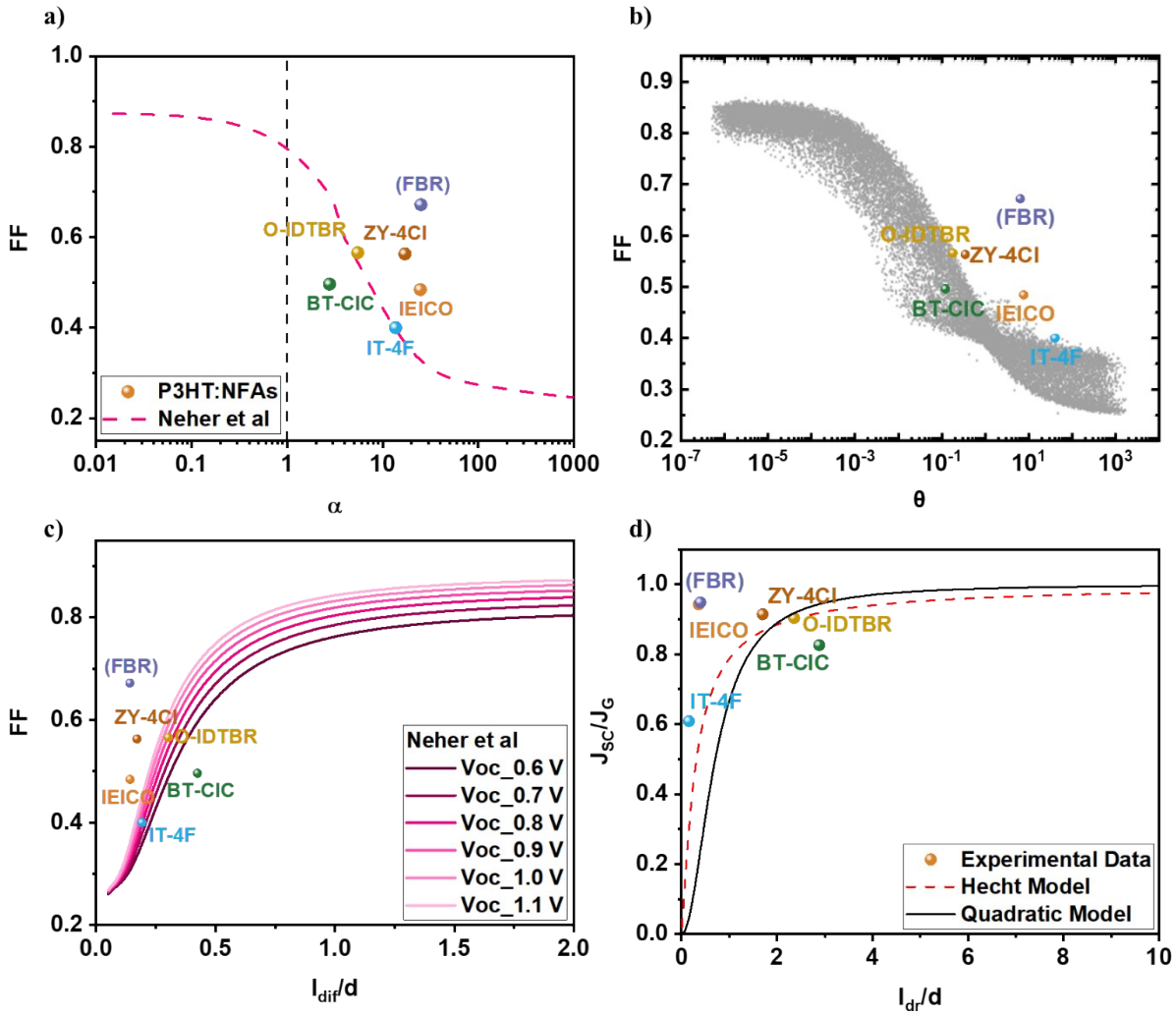

Fig. S28: a) Device FF versus the parameter α as given in equation below for P3HT:NFAs solar cells. Dashed pink line is the analytical model according to the modified Shockley model by Neher et al. b) FF versus θ for the simulated (small, grey symbols) taken from Neher et al data base[23] and the experimental data (sphere colored symbols). The grey symbols reproduced from (Bartesaghi, D., Pérez, I. D. C., Kniepert, J., Roland, S., Turbiez, M., Neher, D., & Koster, L. J. A. (2015). Competition between recombination and extraction of free charges determines the fill factor of organic solar cells. *Nature communications*, *6*(1), 7083. Under CC BY 4.0 license https://creativecommons.org/licenses/by/4.0/). c) Correlation of the FF with the relative diffusion length l_{dif}/d for P3HT:NFAs based systems. The continuous lines in (c) are obtained using analytical expressions (see equations below) for the fixed V_{OC} values of 0.6, 0.7, 0.8, 0.9, 1.0, and 1.1 V. d) correlation of the efficiency of charge extraction (J_{SC}/J_G) at the 1-Sun illumination with the effective drift length l_{dr}/d for P3HT:NFAs. The dashed line in (d) is obtained using the Hecht equation and the solid line using quadratic model (see equation below).

Table S9: Parameters calculated under simulated AM1.5G illumination, to study the competition between charge extraction and recombination (α and θ). The carrier diffusion length (l_{dif}) at the J_{SC} condition, and the carrier drift length (l_{dr}), for the studied P3HT:NFAs organic solar cells at the 1 Sun-equivalent illumination.

P3HT:NFAs	**α**	**θ**	l_{dif} **(nm)**	l_{dr} **(nm)**
IT-4F	13.64	40.38	17.80	14.63
BT-CIC	2.77	0.12	47.95	325.89
IEICO	24.76	7.60	27.85	71.07
ZY-4Cl	17.06	0.34	13.69	136.07
FBR	25.07	6.34	14.12	39.71
O-IDTBR	5.46	0.17	24.19	188.57

Equations used to calculate the figure of merit α:[24]

$$\alpha^2 = \frac{q\gamma d^3 J_G}{4\mu_n\mu_p (k_B T)^2}$$

$$FF = \frac{u_{oc} - ln(0.79 + 0.66u_{oc}^{1.2})}{u_{oc} + 1}$$

$$u_{oc} = \frac{qV_{oc}}{(1+\alpha)k_B T}$$

Where, q is the primery charge, γ is the bi-molecular recombination rate from TDCF, d is the photoactive layer thickness, J_G is the generation current (~J_{sat}), $\mu_n\mu_p$ electron and hole mobility, respectively, $k_B$is Boltzmann constant, and T room temperature.

To calculate θ we used equations below:[23]

$$\theta = \frac{\gamma G d^4}{\mu_n\mu_p V_{int}^2} \propto \frac{k_{rec}}{k_{ex}}$$

$$V_{int} = \frac{LUMO_A - HOMO_D}{q} - 0.4V$$

$$G = \frac{J_{sc}}{qd}$$

Where, G is generation rate.

To calculate the diffusion length (l_{dif}) from α:[25]

$$\alpha = \sqrt{\frac{q^2\gamma G d^4}{4\mu^2(k_B T)^2}} = \sqrt{\frac{q^2 d^4}{4(\mu k_B T\tau)^2}} = \frac{d^2}{2D\tau} = \left(\frac{d}{\sqrt{2}l_{dif}}\right)^2$$

Where, τ is the carrier recombination lifetime.

To calculate diffusion length (l_{dr}) from θ:[25]

$$\theta = \frac{\gamma G d^4}{\mu_n \mu_p V_{int}^2} = \frac{d^4}{\mu^2\tau^2 V_{int}^2} = \left(\frac{d^2}{\mu\tau V_{int}}\right)^2 = \left(\frac{d}{l_{dr}}\right)^2$$

Hecht equation:

$$\frac{J_{sc}}{J_G} = \frac{2l_{dr}}{d}\left(1 - exp\left(-\frac{d}{2l_{dr}}\right)\right)$$

Quadratic model:

$$\frac{J_{sc}}{J_G} = \frac{1}{1 + \frac{1}{28}\left(\frac{d}{l_{dr.eff}}\right)^2} = \frac{2\left(\frac{l_{dr}}{d}\right)^2}{1 + 2\left(\frac{l_{dr}}{d}\right)^2}$$

Atomic force mircoscopy (AFM)

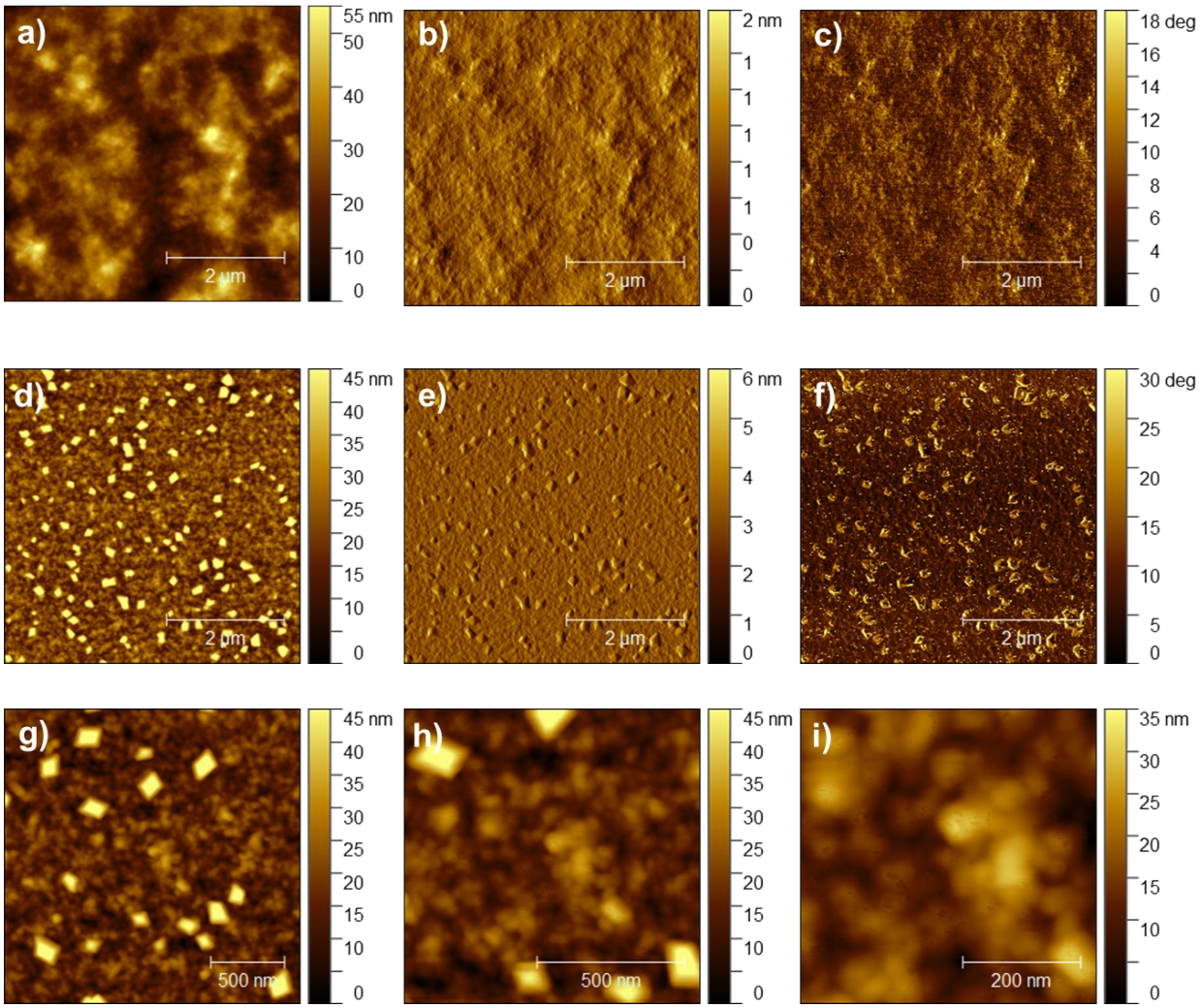

Fig. S29: AFM images of a selection of systems (a-c) P3HT:IT-4F, (d-i) P3HT:ZY-4Cl. Where (a, d, g, h, and i) represent topography, (b) and (e) represent amplitude, (c) and (f) represent phase images.

Transmission Electron Microscope (TEM) and Electron Energy Loss Spectroscopy (EELS)

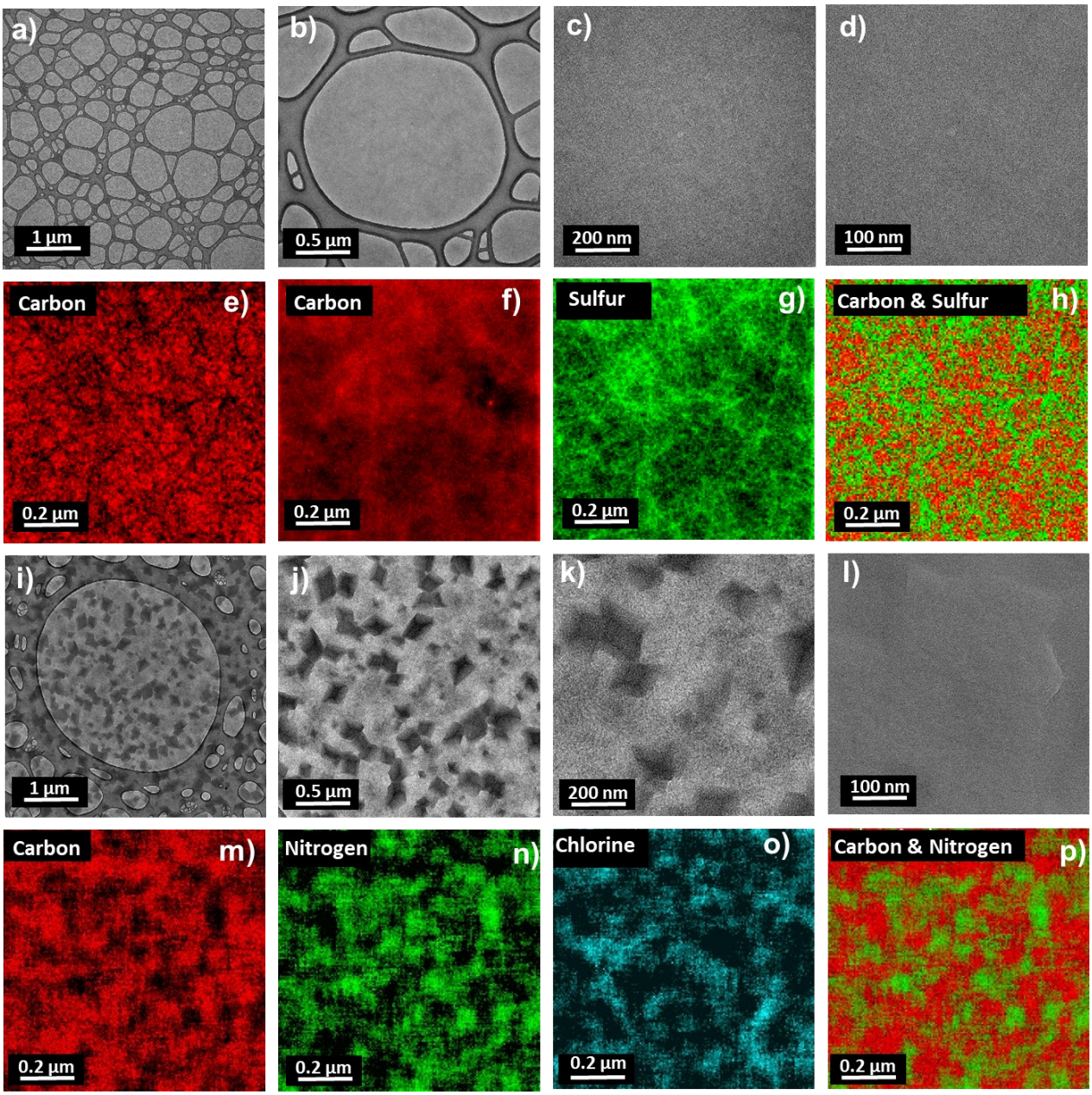

Fig. S30: (a, b, c, and d) TEM analysis of thin film morphology for P3HT:IT-4F. (e, f, g, and h) the EELS maps that depict the donor rich (green)- acceptor rich (red) phases. (i, j, k, and l) TEM images of P3HT:ZY-4Cl. (m, n, o, and p) the EELS maps that depict the donor rich (red)- acceptor rich (green) phases.

Outdoor Stability

P3HT:NFAs-based devices were first soldered with solar ribbons (Ulbrich Solar Technologies) to extend their electrodes. The devices were then sandwiched between two layers of tempered glass and two layers of encapsulants made of thermoplastic polyurethane. Butyl rubber edge sealant (PVS 101) was applied to prevent moisture ingress from the sides of the device. The stack was vacuum laminated in an Ecolam5 Ecoprogetti laminator at 120°C for 15 minutes. For outdoor stability measurements, the encapsulated devices were mounted at KAUST in a hot desert climate with a tilt angle of 25° and a south-facing orientation. The devices were masked with black tape, and J-V scans were performed approximately every 10 minutes during the daytime. Solar irradiance was recorded using a calibrated pyrometer (EKO MS-80). The devices were monitored under maximum power point tracking (MPP) by TUV Rheinland, and IV curves were recorded every 10 minutes. Data acquisition was performed using EKO's MP160 software.

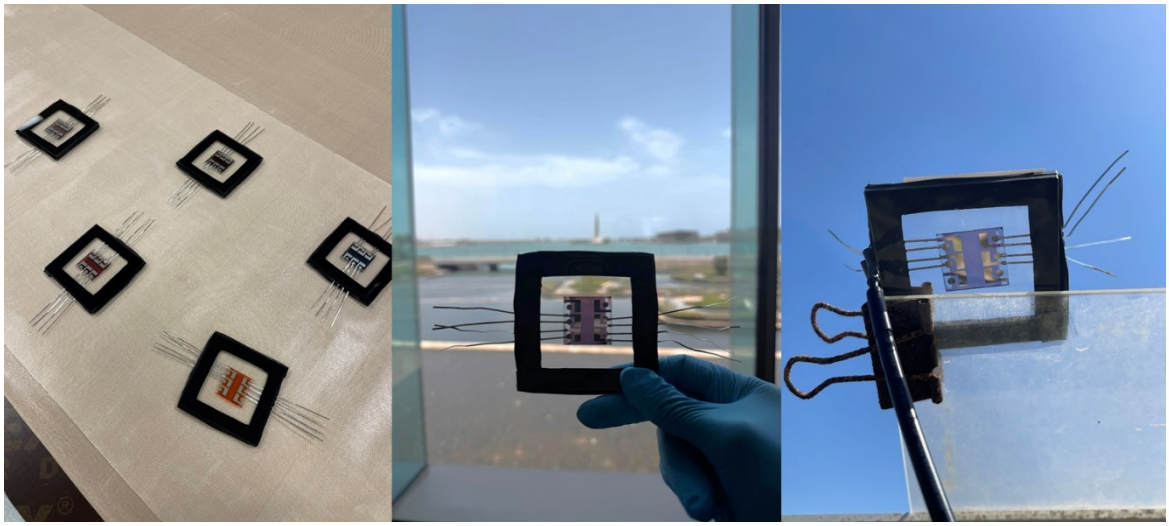

Fig. S31: P3HT:NFAs encapsulated devices for outdoor stability measurenments from the test site at KAUST, Thuwal, Saudi Arabia.

References

1. Algar, W. R., Kim, H., Medintz, I. L. & Hildebrandt, N. Emerging non-traditional Förster resonance energy transfer configurations with semiconductor quantum dots: Investigations and applications. *Coordination Chemistry Reviews* vols 263–264 65–85 Preprint at https://doi.org/10.1016/j.ccr.2013.07.015 (2014).
2. Firdaus, Y. *et al.* Long-range exciton diffusion in molecular non-fullerene acceptors. *Nat Commun* **11**, (2020).
3. Lin, J. D. A. *et al.* Systematic study of exciton diffusion length in organic semiconductors by six experimental methods. *Mater Horiz* **1**, 280–285 (2014).
4. Gong, J. & Krishnan, S. Mathematical modeling of dye-sensitized solar cells. in *Dye-Sensitized Solar Cells: Mathematical Modelling, and Materials Design and Optimization* 51–81 (Elsevier, 2019). doi:10.1016/B978-0-12-814541-8.00002-1.
5. Karuthedath, S. *et al.* Intrinsic efficiency limits in low-bandgap non-fullerene acceptor organic solar cells. *Nat Mater* **20**, 378–384 (2021).
6. Sun, Y., Han, Y. C. & Liu, J. G. Controlling PCBM aggregation in P3HT/PCBM film by a selective solvent vapor annealing. *Chinese Science Bulletin* **58**, 2767–2774 (2013).
7. Spano, F. C., Clark, J., Silva, C. & Friend, R. H. Determining exciton coherence from the photoluminescence spectral line shape in poly(3-hexylthiophene) thin films. *Journal of Chemical Physics* **130**, (2009).
8. Piris, J. *et al.* Photogeneration and ultrafast dynamics of excitons and charges in P3HT/PCBM blends. *Journal of Physical Chemistry C* **113**, 14500–14506 (2009).
9. Benatto, L. *et al.* FRET–Calc: A free software and web server for Förster Resonance Energy Transfer Calculation. *Comput Phys Commun* **287**, (2023).
10. Khan, J. I. *et al.* P3HT Molecular Weight Determines the Performance of P3HT:O-IDTBR Solar Cells. *Solar RRL* **3**, (2019).
11. Kabongo, G. L. *et al.* Photoluminescence Quenching and Enhanced Optical Conductivity of P3HT-Derived Ho3+-Doped ZnO Nanostructures. *Nanoscale Res Lett* **11**, (2016).
12. Mauer, R., Kastler, M. & Laquai, F. The impact of polymer regioregularity on charge transport and efficiency of P3HT:PCBM photovoltaic devices. *Adv Funct Mater* **20**, 2085–2092 (2010).
13. Würfel, U. & Unmüssig, M. Apparent Field-Dependence of the Charge Carrier Generation in Organic Solar Cells as a Result of (Bimolecular) Recombination. *Solar RRL* **2**, (2018).
14. science.287.5454.839.
15. Gorenflot, J. *et al.* Detailed study of N,N′-(diisopropylphenyl)-terrylene-3,4:11,12-bis(dicarboximide) as electron acceptor for solar cells application. in *Synthetic Metals* vol. 161 2669–2676 (2012).
16. Jaumot, J., Gargallo, R., De Juan, A. & Tauler, R. A graphical user-friendly interface for MCR-ALS: A new tool for multivariate curve resolution in MATLAB. *Chemometrics and Intelligent Laboratory Systems* **76**, 101–110 (2005).
17. Jaumot, J., de Juan, A. & Tauler, R. MCR-ALS GUI 2.0: New features and applications. *Chemometrics and Intelligent Laboratory Systems* **140**, 1–12 (2015).
18. de Juan, A. & Tauler, R. Multivariate Curve Resolution-Alternating Least Squares for Spectroscopic Data. in *Data Handling in Science and Technology* vol. 30 5–51 (Elsevier Ltd, 2016).
19. HOWARD, I. A., MANGOLD, H., ETZOLD, F., GEHRIG, D. & LAQUAI, F. TRANSIENT ABSORPTION DATA ANALYSIS BY SOFT-MODELLING. in 53–78 (World Scientific Pub Co Pte Lt, 2014). doi:10.1142/9789814556927_0004.

20. Wu, J. *et al.* Effects of conjugated bridges on the photovoltaic properties of: Ortho - functionalized perylene diimides for non-fullerene polymer solar cells. *J Mater Chem C Mater* **6**, 13171–13178 (2018).
21. Saggar, S. *et al.* Impact of Polymer Molecular Weight on Polymeric Photodiodes. *Adv Opt Mater* **10**, (2022).
22. Yang, C. *et al.* Molecular design of a non-fullerene acceptor enables a P3HT -based organic solar cell with 9.46% efficiency. *Energy Environ Sci* **13**, 2864–2869 (2020).
23. Bartesaghi, D. *et al.* Competition between recombination and extraction of free charges determines the fill factor of organic solar cells. *Nat Commun* **6**, (2015).
24. Neher, D., Kniepert, J., Elimelech, A. & Koster, L. J. A. A New Figure of Merit for Organic Solar Cells with Transport-limited Photocurrents. *Sci Rep* **6**, (2016).
25. Tokmoldin, N. *et al.* Explaining the Fill-Factor and Photocurrent Losses of Nonfullerene Acceptor-Based Solar Cells by Probing the Long-Range Charge Carrier Diffusion and Drift Lengths. *Adv Energy Mater* **11**, (2021).